

Fig. II.59. UN. **(a)** The low-temperature resistivity of neutron irradiated, plasma-jet-fused UN ($a_0 = 0.48896(8)$ nm) using a variety of fission doses indicated in the figure [80TOMM]. **(b)** Relative change of lattice parameter, $\Delta a/a$, resistivity, $\Delta\rho/\rho$, and Néel temperature, T_N , as a function of irradiation dose. Note the reverse behaviour of T_N against a and ρ .

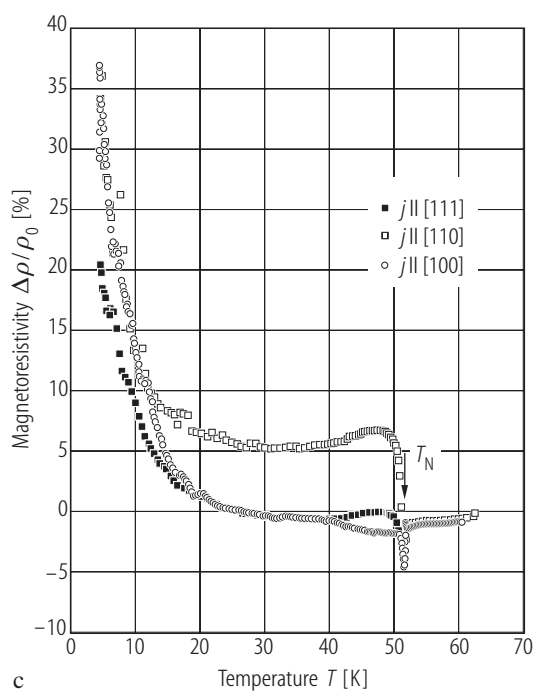


Fig. II.60. UN s.c. Resistance, R , vs. temperature, T , measured at $B = 0$ and 8 T along three main crystallographic axes (panels a). Transverse magnetoresistivity $\Delta\rho/\rho_0$ vs. T around T_N taken in a magnetic field of 8 T (panels b) [05DTSM]. Note a small shift in T_N ($B = 0$) to lower temperatures at $B = 8$ T (sharp minimum). Transverse magnetoresistivity, $\Delta\rho/\rho_0$, vs. temperature, T , up to 65 K taken along three main crystallographic axes in a magnetic field $B = 8$ T (panel c) [05DTSM]. If $\Delta\rho/\rho_0$ for $j \parallel [110]$ is positive in the whole temperature range below T_N , then this quantity for $j \parallel [100]$ and $[111]$ changes its sign at 25 K becoming positive below this temperature. Note that also for these two directions $\Delta\rho/\rho_0$ reaches the highest value of about 40% at 4.2 K almost double the value measured along $[111]$.

For Fig. II.60a, b see next page

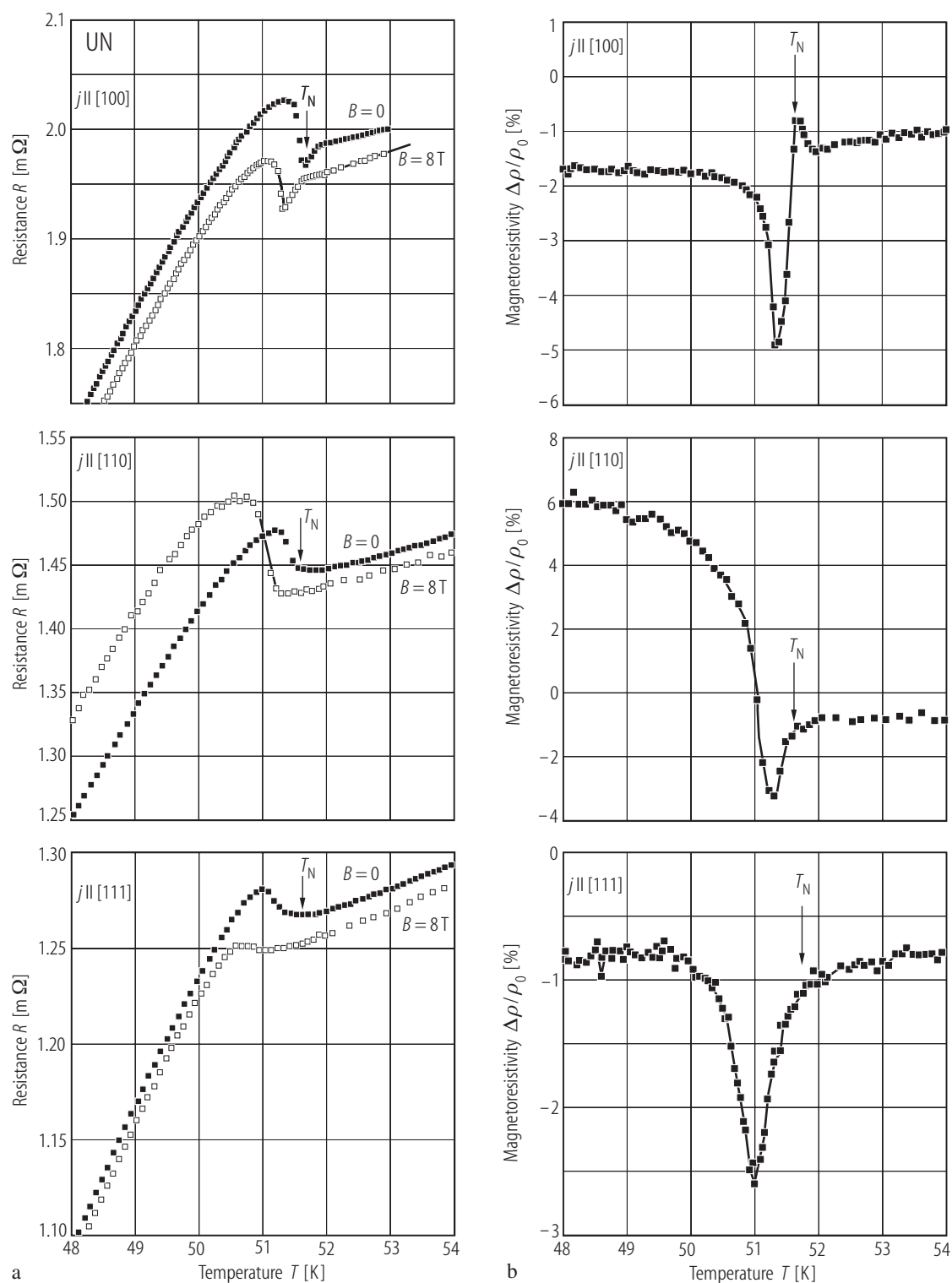


Fig. II.60 a, b. For caption see previous page.

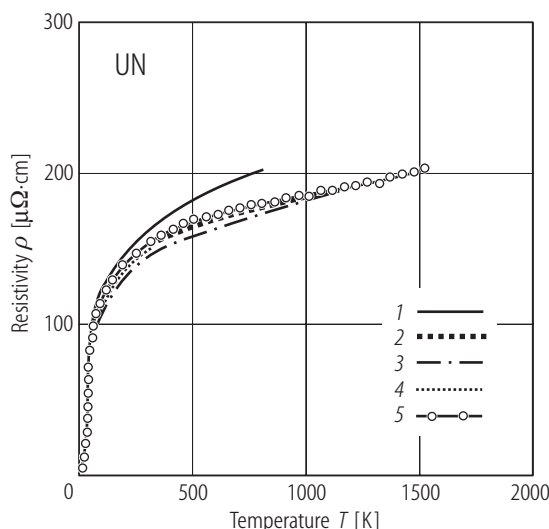


Fig. II.61. UN. Electrical resistivity, ρ , vs temperature, T , up to 1600 K measured by various researchers: 1 [72DC], 2 [64KMGF], 3 [72OKN], 4 [70MFM] and 5 [83T]. For the electrical resistivity correlation, applicable for temperatures $298 \leq T < 1600$ K see ref. [90HTP3].

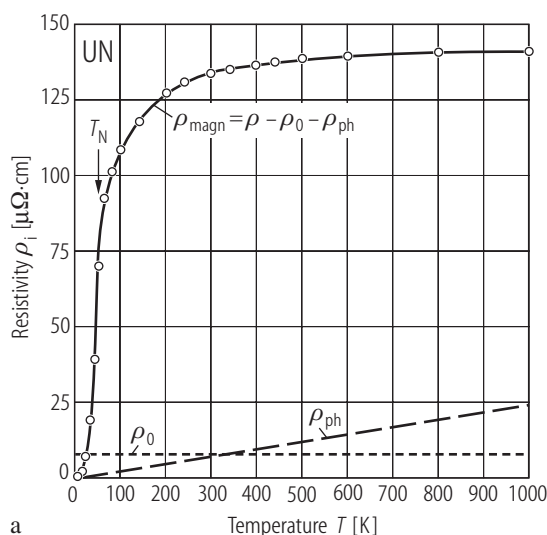


Fig. II.62. UN sintered. (a) Components of HT-electrical resistivity ρ_0 , ρ_{ph} , and ρ_{magn} vs. T up to 1000 K and (b) thermoelectric power, S , vs. T of the UN sample sintered at 2600 K in 1 atm of nitrogen ($a_0 = 0.488917(15)$ nm) [70MFM]. The results were corrected to theoretical density. The magnetic part, ρ_{magn} , fits from 10 to 52 K the equation: $\rho_{magn} = 6.15 \cdot 10^{-3} T^{2.38(8)} \mu\Omega\text{cm}$ and between 800 and 1300 K

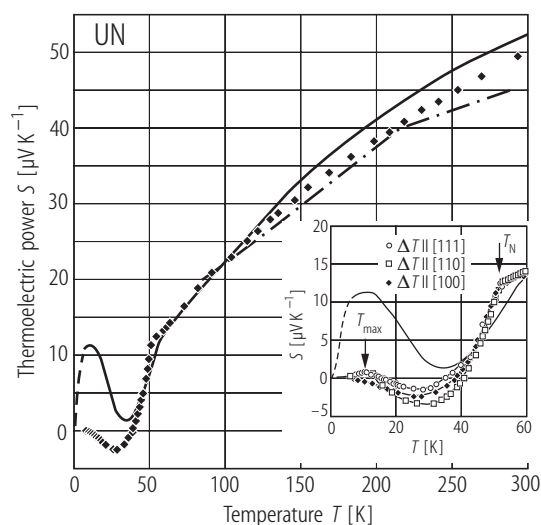
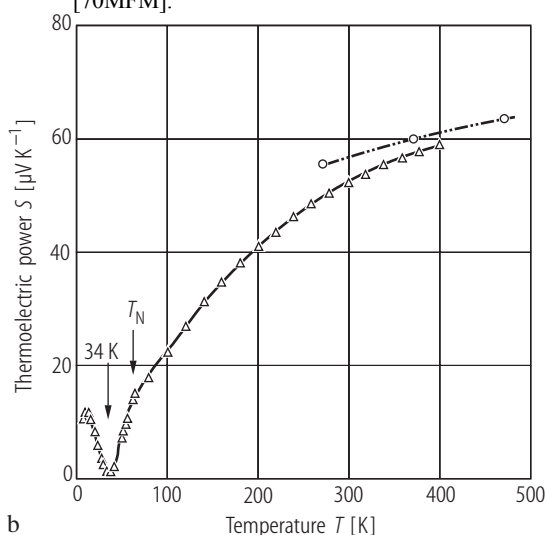


Fig. II.63. UN s.c. [100]. Thermoelectric power, S , vs. temperature, T , measured along the [100] crystallographic direction (symbols) [05DTSM]. Note a high S -value of $\sim 50 \mu\text{V/K}$ at RT for gradient, ΔT , applied along [100] and a small negative minimum in $S(T)$ at 26 K. These data are in good agreement with those found on the sintered samples of UN (solid line [70MFM] and dot-dashed line [72OKN]), which are presented in the wide temperature range in Fig. II.62b and in Fig. I.35. The thermopower measured along the remaining directions [110] and [111] within experimental error has a very similar temperature dependence (not shown for clarity). The inset shows the low-temperature behaviour of S for three main crystallographic directions and polycrystalline data of [70MFM].



reaches a constant value ρ_∞ of $142.4 \mu\Omega\text{cm}$. The minimum in S at 34 K and a local maximum at 10 K are caused by magnon and phonon drags or their combination. Compare these results with those obtained on a single crystal, which are given in Fig. II.65. The high-temperature data (open circles) are from [64WP].

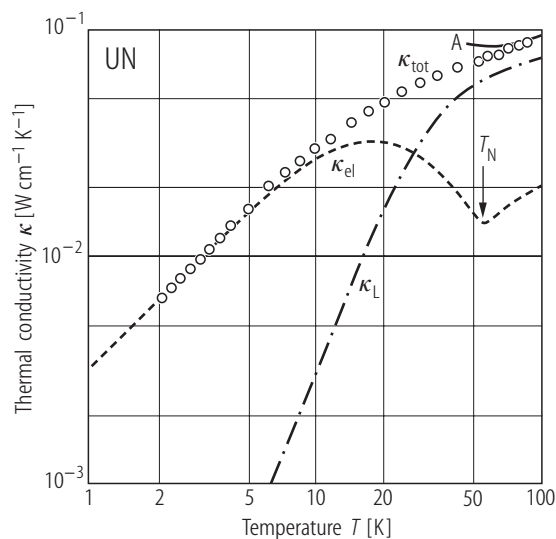


Fig. II.64. UN. Thermal conductivity, κ , vs. temperature, T , (open circles) on a double logarithmic plot [69RW]. Curve A is smoothed result of [70MFM]. κ_{el} and κ_{L} are the components of the total κ_{tot} , i.e. κ_{el} (dashed) and κ_{L} (dot-dashed) are derived values of the electronic thermal conductivity and of the lattice thermal conductivity, respectively. $T_{\text{N}} = 53$ K. Note that below 5 K the heat is transported primarily by electrons, whereas phonons predominate at higher temperatures.

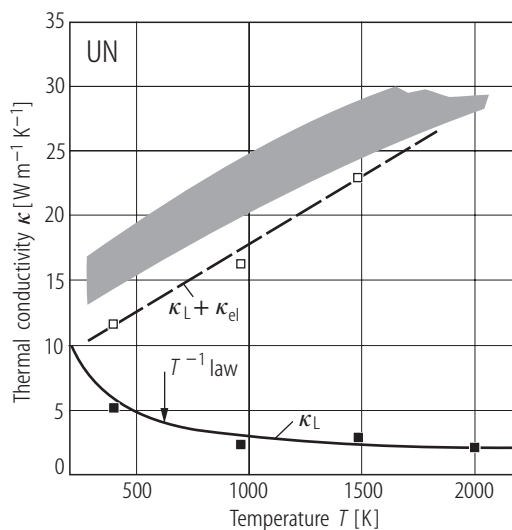


Fig. II.66. UN. The high-temperature (300...2000 K) lattice thermal conductivity, κ_{L} , calculated by the MD method vs. T (closed squares). κ_{el} was found from the Wiedemann-Franz law using $\rho(T)$ from [90HTP1]. The sum $\kappa_{\text{L}} + \kappa_{\text{el}}$ (open squares) was compared to the experimental κ_{tot} results obtained by a large number of various authors (shaded area) who are listed in the original paper [00KYYU3]. Note that the calculated κ_{L} values follow the $1/T$ law. The difference between the experimental κ_{tot} and calculated κ_{L} values to a large extend is thus supposed to be due to the electronic contribution κ_{el} , which completely predominates at higher temperatures.

For Fig. II.65 see next page

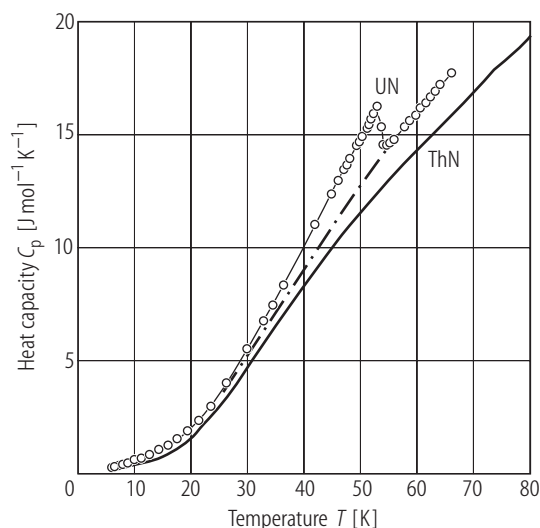


Fig. II.67. UN. Heat capacity, C_p , vs. temperature, T , in the region of antiferromagnetic order, measured between 5.7...67 K (open circles) [66WB]. $T_{\text{N}} = 52$ K. The dot-dashed curve is the estimate of the lattice heat capacity (see the text). Compare it with measurements on ThN [72DDD] (solid line).

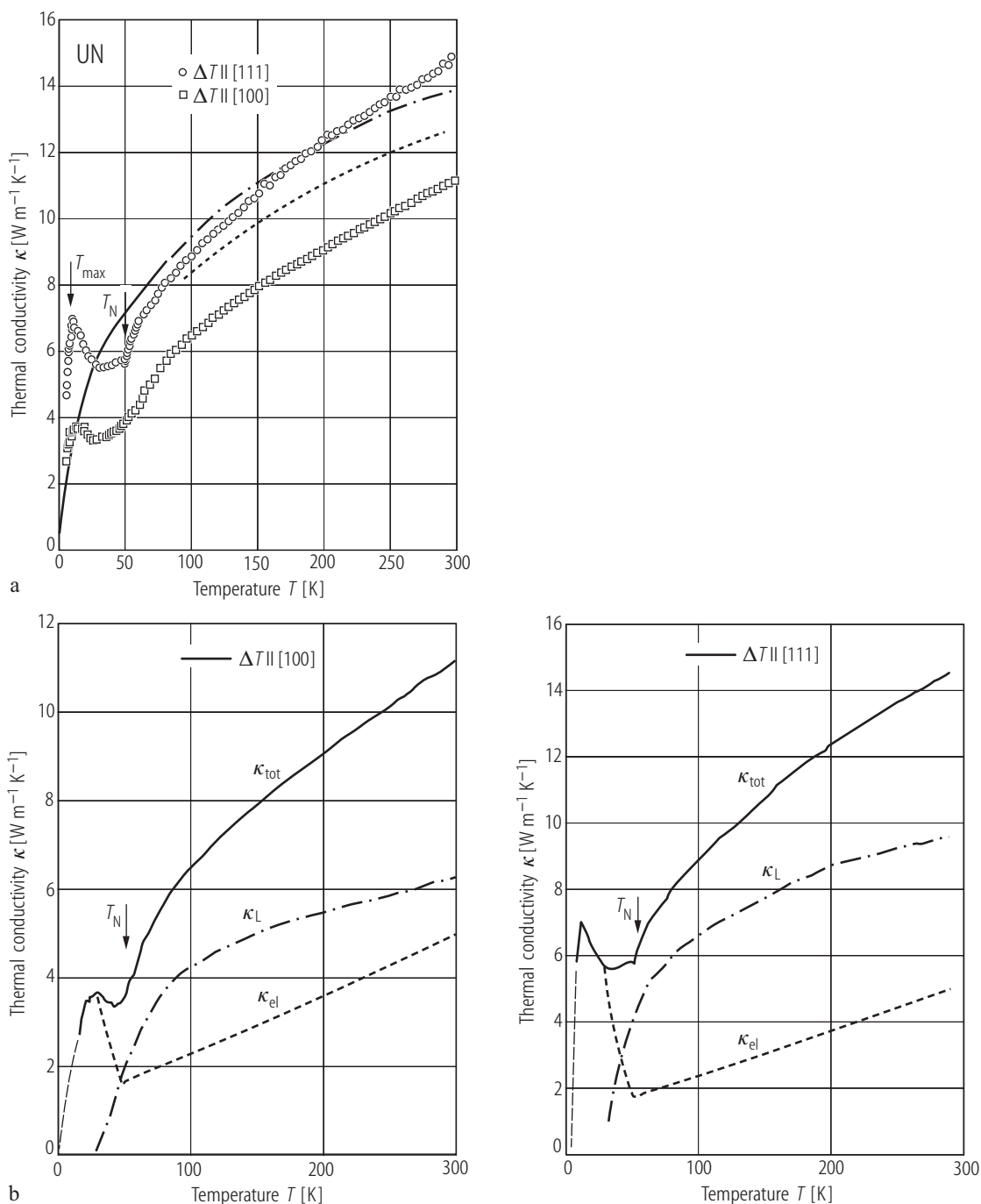


Fig. 11.65. UN s.c. **(a)** Thermal conductivity, κ , vs. temperature, T , measured for the gradient, ΔT , applied along two crystallographic axes [100] and [111] [05DTSM]. There is seen some anisotropy in $\kappa(T)$, but the temperature runs for these two directions very similar. Note a distinct change in $\kappa(T)$ at T_N and peaking this dependence at about $T_{\text{max}} = 13$ K, which was not observed in low-temperature measurements of the polycrystalline sample (solid curve) [69RW]. Note that the polycrystalline results found at

higher temperatures (chain curve by [70MFM] and dotted curve by [74KTM2]) behave in similar way like the single-crystalline ones. **(b)** κ vs. T . The electron thermal conductivity, κ_{el} , (dashed curves) was estimated on the basis of the Wiedemann-Franz law from $\rho(T)$ of UN single crystal measured in two crystallographic directions [100] (lhp) and [111] (rhp). Correspondingly, the phonon contributions κ_L (chain curves) were determined as a difference: $\kappa_L = \kappa_{\text{tot}} - \kappa_{\text{el}}$.

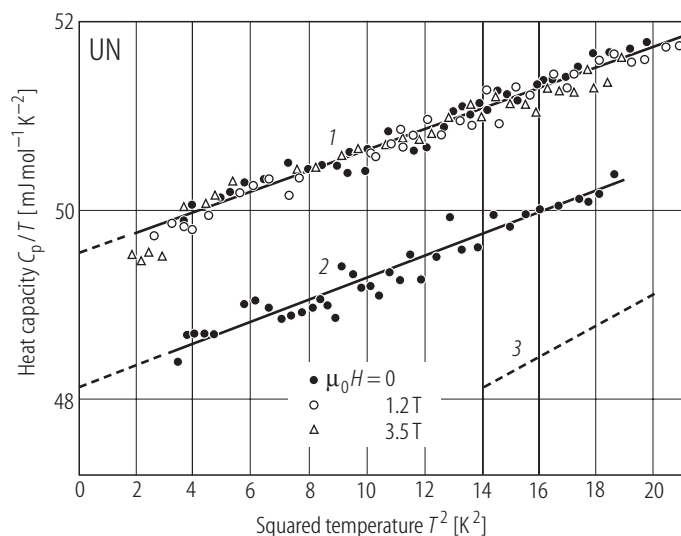


Fig. II.68. UN. The plot C_p/T vs. T^2 measured between 1.3 and 4.6 K for the samples being: 1) heat treated in N_2 at 2250 °C and 2) without heat treatment [68SDFB]. The respective $\gamma(0)$ and Θ_D values were found: for sample 1 ($a_0 = 0.48888(1)$ nm): 49.58(10) mJ/mol K² and 324(7) K, for sample 2: 48.14(16) mJ/molK² and 322(13) K, respectively. No change of C_p in magnetic fields up to 3.5 T has been noted. 3) Extrapolated high-temperature data of [66WB].

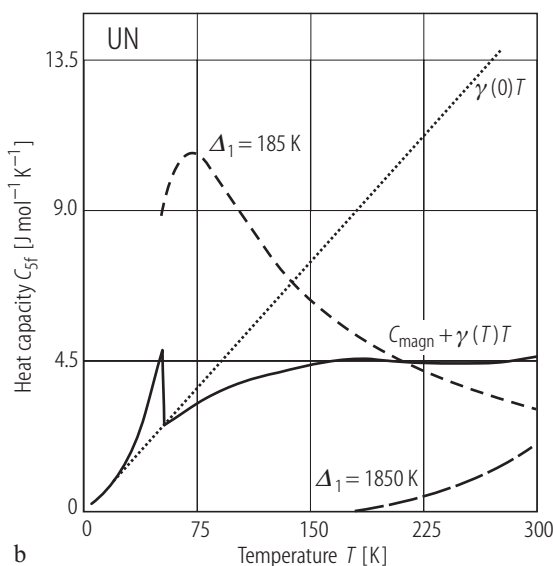
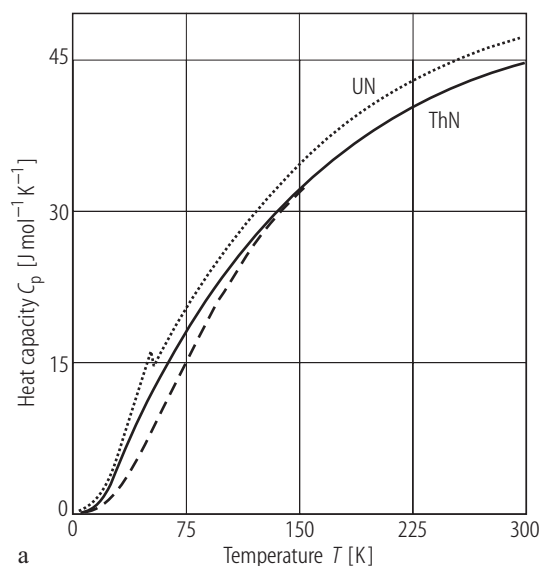


Fig. II.69. UN (ThN). **(a)** Experimental heat capacity, C_p , vs. T for ThN (solid curve) [72DDD], compared to that of UN (dotted curve) [66WB]. The former curve is well approximated by two terms, i.e. by the phonon acoustic and optic modes, associated with the respective Debye and Einstein functions, respectively. $\Theta_D = 291$ K and $\Theta_E = 495$ K. $(C_p - C_V)_d = 0.71 \cdot T$ mJ/mol K² (see Fig. II.7). The dashed curve is approximated only by the former one.

(b) Estimated magnetic and electronic parts of heat capacity, C_{sf} vs. T for UN [72DDD]. Dashed curves indicate the Schottky contribution originated from the U^{4+} ion in the presence of the crystal field effect. Δ_1 gives the energy separation between Γ_1 and Γ_2 levels (see [78LL2]). Note that the electronic heat capacity $C_{el} (= \gamma(0) \cdot T)$ severely exceeds the $C_{mag}(T)$ curve for temperatures $T > T_N$ with $\gamma(0) \approx 50$ mJ/K² mol.

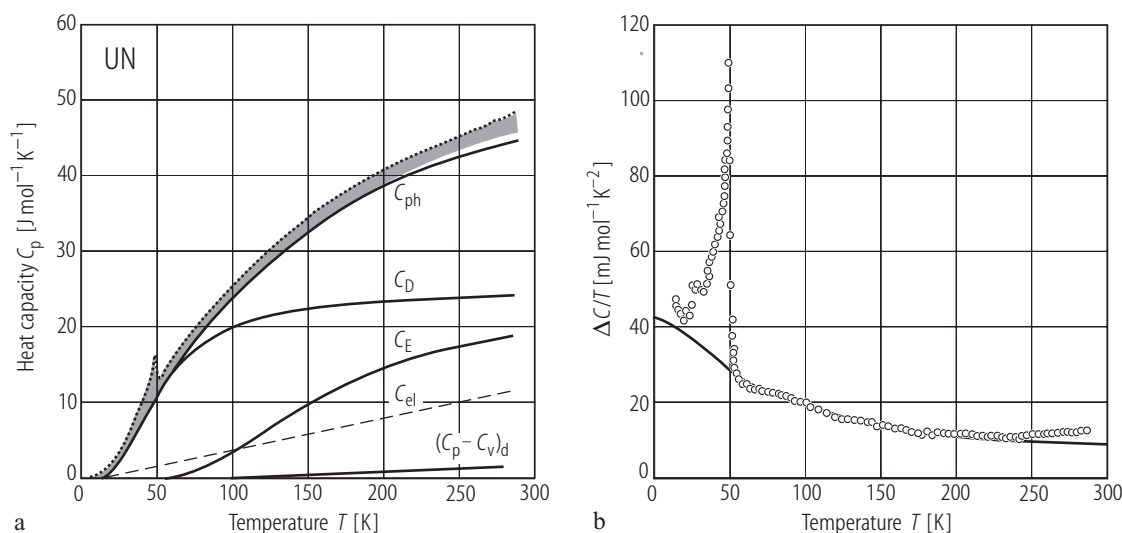


Fig. II.70. UN. **(a)** Heat capacity, C_p , vs. temperature, T , [90YS]. The dotted and solid lines indicate respectively the measured C_p for UN and calculated phonon part $C_{ph} = C_D(\Theta_D) + C_E(\Theta_E) = C_p - \Delta C - (C_p - C_v)_d$, where ΔC (shaded area) is the sum of magnetic C_{magn} and electronic C_{el} contribution. $\Theta_D (= 225 \text{ K})$ and $\Theta_E (= 530 \text{ K})$ are the Debye and Einstein temperatures, respectively. The anharmonic term $(C_p - C_v)_d = AC_p^2 T$ where $A = 244 \cdot 10^{-6} \text{ mol/J}$ was found from RT data of C_p , the bulk thermal expansion and the isothermal compressibility κ . Note that $C_{el} (= \gamma(0)T)$ calculated by using $\gamma(0) (= 41 \text{ mJ/mol K}^2)$ predominates any values of ΔC . Therefore, $\gamma_0 (= 5 \text{ mJ/mol K}^2)$ has been used. **(b)** The plot $\Delta C/T$ vs. T , where ΔC is the sum of magnetic and electronic contribution [90YS]. The solid line represents the calculated contribution based on the band model [86YLS] assuming the Lorentzian DOS for 5f electrons: $N(E) = N_0/(1+E/\Delta)^2$. $N_0 = 1.3 \cdot 10^{-3} \text{ K}^{-1}$, $\Delta = 200 \text{ K}$. The electronic part was established assuming $\gamma_0 = 5 \text{ mJ/K}^2 \text{mol}$ instead of $\gamma(0) = 41 \text{ mJ/K}^2 \text{mol}$ at $T = 0 \text{ K}$. The bandwidth, Δ , corresponds to the energy gap δ of the $\Gamma_1 - \Gamma_4$ crystal field scheme. This was reported to be 177 K from the magnetic properties [78LL2] and 185 K [72DDD] from the specific heat (see Fig. II.69).

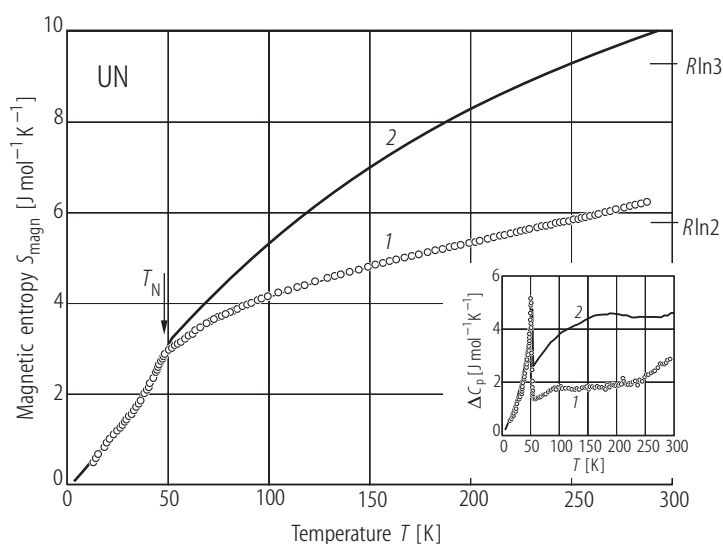


Fig. II.71. UN. Magnetic entropy, S_{magn} , calculated for two cases: (1) from the difference in C_p of UN [66WB] and ThN [72DDD] and (2) from the difference of C_p and determined phonon contribution, C_{ph} , in [90YS]. The inset shows ΔC_p vs. T obtained for these two cases.

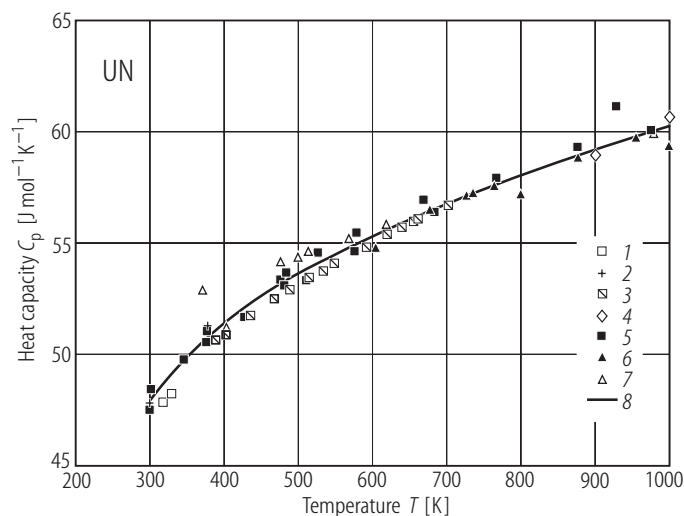


Fig. II.72. UN. Heat capacity, C_p , vs. temperature, T , up to 1000 K measured by various authors: 1 [66CDM], 2 [66WB], 3 [71CM], 4 [70A], 5 [71TMAM], 6 [79FKWM], 7 [72OL] and empirically correlated by 8 [90HTP4] (solid line).

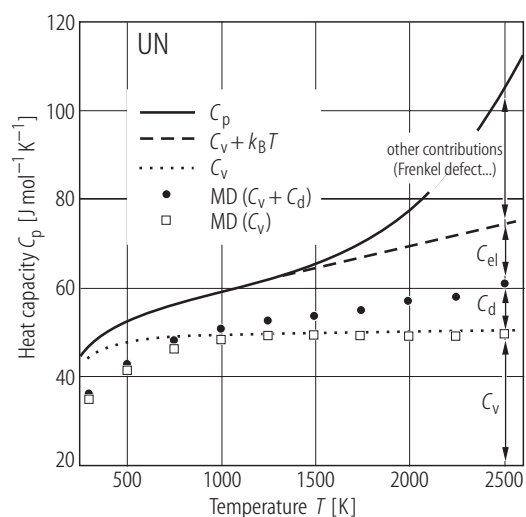


Fig. II.73. UN. Heat capacity, C_p vs. temperature, T , (solid curve). Data measured in the ranges $298 \leq T \leq 2628$ K by different authors and correlated according to the Einstein theory with adding some high-temperature modification to the model to explain the upward turn above 2000 K. $\Theta_E = 367.5$ K (see [90HTP4]). Based on this, the correlations of the enthalpy, entropy, Gibbs free energy and free energy functions were also derived. The open squares and closed circles are the results of MD calculations [00KYYU1] without and with the lattice dilatational contribution ($C_d = AT$, where A is an empirically determined constant, $C_d/T = 3.71$ mJ/mol K²). The theoretical expression for $A = \alpha^2 V / \kappa$, V is the molar volume, κ is the compressibility, α is the linear expansion coefficient so the partly solid and partly dashed curve can be described as: $C_p = C_v + C_d + C_{el}$. The electronic contribution $C_{el} = \gamma T$ was determined as the difference between the MD ($C_v + C_d$) data and the reported C_p data (solid/dashed curve). This yields γ (700...2500 K) = 6.32 mJ/mol K² considerably lower than $\gamma(0)$ (= 35 mJ/mol K²) [66CDM] or about 50 mJ/mol K² [68SDFB]. The large increase in the experimental data of C_p from 1500 K cannot be explained by the MD calculation (see [90HTP4]).

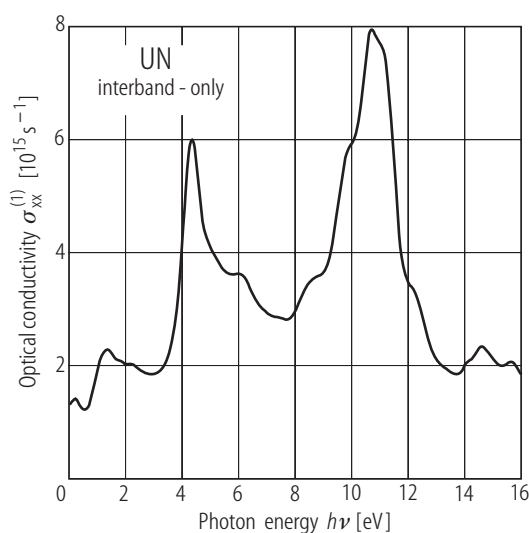
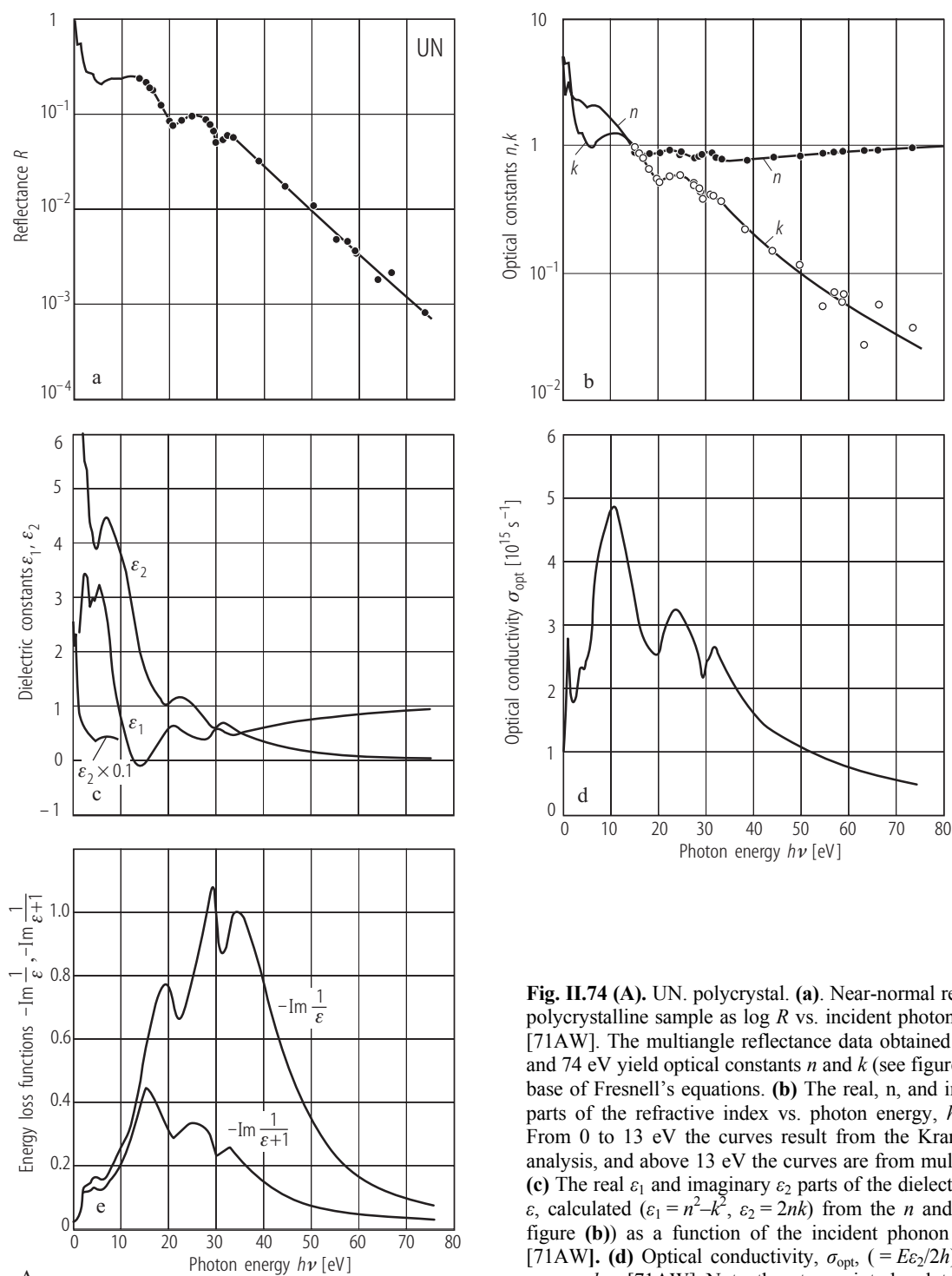


Fig. II.75. UN. Calculated optical conductivity, $\sigma_{xx}^{(1)}$, vs. photon energy, $h\nu$, [050]. The calculated spectrum does not agree with the experiment on polycrystalline sample (see Fig. II.74A). However, the trend of the peaks in the spectrum is consistent with that found for UP, UAs and USb (see Fig. R.43).

For Fig. II.74 see next page



A

10.5, 24.0, and 32.0 eV. The sharp structure seen at 1 eV indicates the single electron transitions. Comparing a strong PE peak at E_F with self-consistent cluster calculations [79EK2] and with the photon energy dependence it appears that the peak may be an initial f-state since a final state is rather a d-band [84S3]. **(e)** Energy-loss functions vs. incident photon energy, $h\nu$, [71AW]. Note peaks at 15, 24, and 32 eV. The two latter are interpreted as the interband transitions, but that at 15 eV is due to surface plasmons.

Fig. II.74 (A). UN. polycrystal. **(a).** Near-normal reflectance of polycrystalline sample as $\log R$ vs. incident photon energy, $h\nu$, [71AW]. The multiangle reflectance data obtained between 13 and 74 eV yield optical constants n and k (see figure **(b)**) on the base of Fresnell's equations. **(b)** The real, n , and imaginary, k , parts of the refractive index vs. photon energy, $h\nu$, [71AW]. From 0 to 13 eV the curves result from the Kramers-Kronig analysis, and above 13 eV the curves are from multiangle data. **(c)** The real ϵ_1 and imaginary ϵ_2 parts of the dielectric constant, ϵ , calculated ($\epsilon_1 = n^2 - k^2$, $\epsilon_2 = 2nk$) from the n and k data (see figure **(b)**) as a function of the incident photon energy, $h\nu$, [71AW]. **(d)** Optical conductivity, σ_{opt} ($= E\epsilon_2/2h$) vs. photon energy, $h\nu$, [71AW]. Note the strong interband transitions at

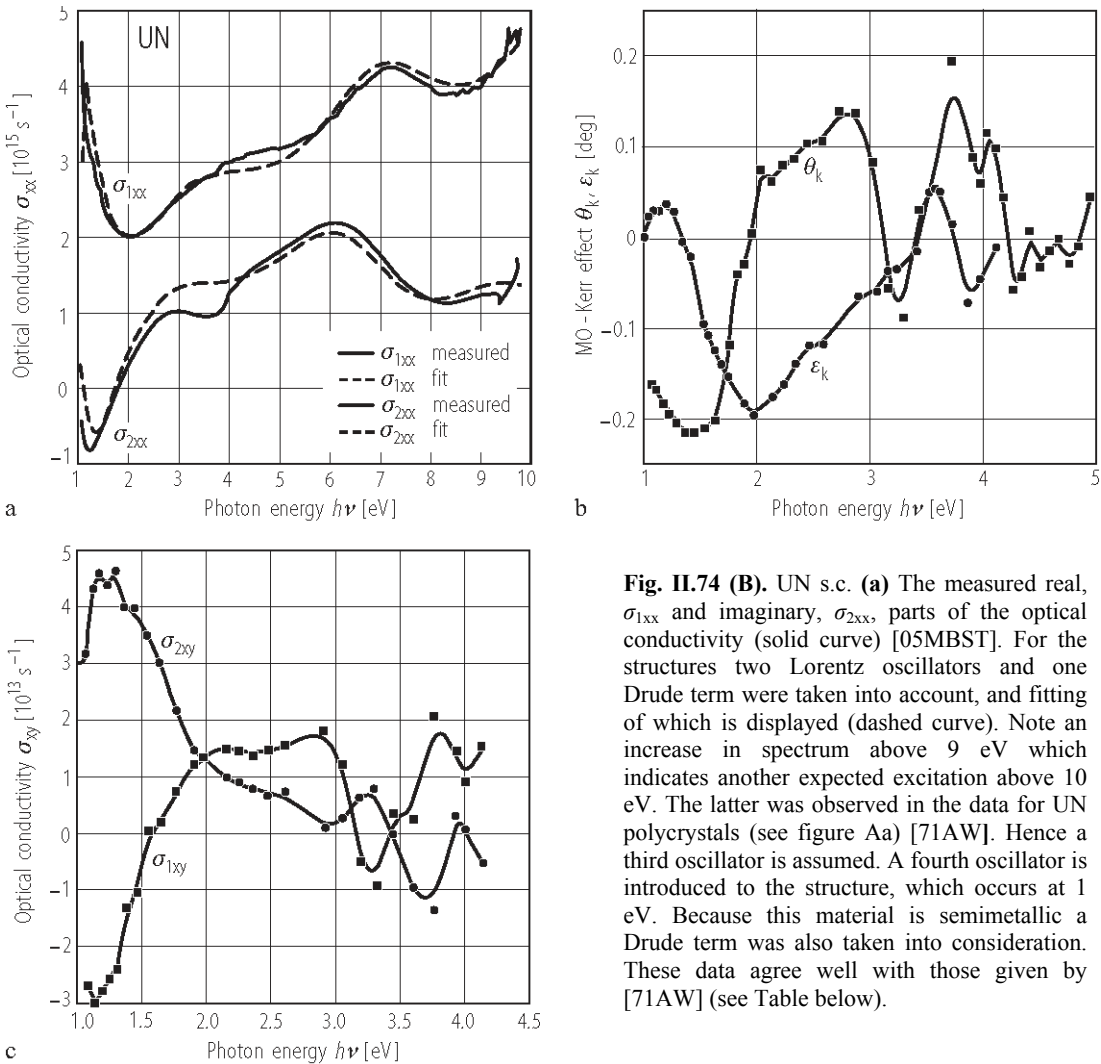


Fig. II.74 (B). UN s.c. (a) The measured real, σ_{1xx} and imaginary, σ_{2xx} , parts of the optical conductivity (solid curve) [05MBST]. For the structures two Lorentz oscillators and one Drude term were taken into account, and fitting of which is displayed (dashed curve). Note an increase in spectrum above 9 eV which indicates another expected excitation above 10 eV. The latter was observed in the data for UN polycrystals (see figure Aa) [71AW]. Hence a third oscillator is assumed. A fourth oscillator is introduced to the structure, which occurs at 1 eV. Because this material is semimetallic a Drude term was also taken into consideration. These data agree well with those given by [71AW] (see Table below).

B

Transition		p-d _{eg}	p-d _{2g}	p _d -f	f-d
	Drude	j = 4	j = 3	j = 2	j = 1
$\hbar\omega_j$ [eV]	0	11.1	7.12	3.79	1.0
f_j	0.43	3.44	1.59	1.57	0.57
$\hbar\gamma_j$ [eV]	10.1	4.78	3.64	4.50	0.75
$\epsilon_{\text{opt}}=1.50$		$\hbar\omega_p=6.87$ eV		$\sum_j f_j=7.60 = Z$	

ω_p is the unscreened plasma frequency, f_j is a phenomenological oscillator strength, Z is the number of electrons in the system, Z_{theor} is 3(N)+6(U) = 9 electrons.

(b) Energy dependence of the MO-Kerr effect, θ_k , measured at $B = 8.2$ T and $T = 54$ K (maximum of magnetization) and ellipticity, ϵ_k , [05MBST]. Note a large structure at 1...2 eV and another one at 3...4 eV in the θ_k vs. $h\nu$ curve. The Kerr rotation and ellipticity is combined with the optical spectrum (figure Ba) to compute the off-diagonal elements of the optical conductivity σ_{xy} (see Fig. Bc). (c) Off-diagonal elements of the optical conductivity σ_{xy} [05MBST]. The structure at 1 eV is connected with the narrow f-band near E_F and the d-conduction band, similar as for other uranium mononitrides (compare it with those structures presented by [80S2] and [84RSV]).

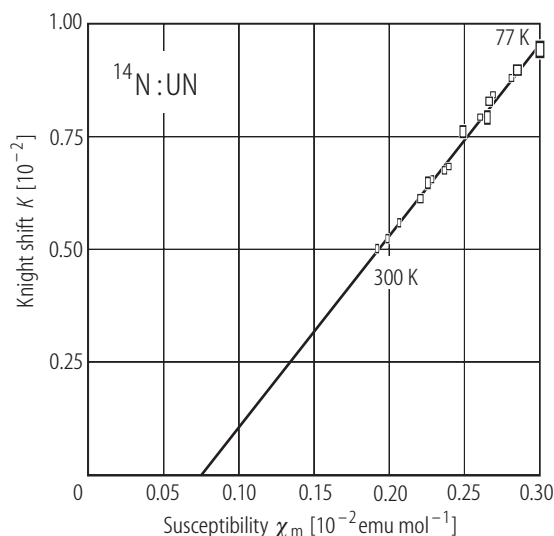


Fig. II.76. UN. Knight shift, K , in the paramagnetic state of ^{14}N vs. molar susceptibility, χ_m , where the temperature is an implicit variable [69K]. K is a linear function of χ_m taken from [62TTL] and [64AJD]: $K = K_0 + \alpha\chi_m$ where $K_0 = -(31.5(35) \cdot 10^{-4})$ and $\alpha = 4.20(25) \text{ mol/emu}$. From the latter value the exchange constant J_{sf} ($\approx -1.0(2) \text{ eV}$) has been inferred. The line width is composed of several contributions. The magnetic contribution $\Delta H_{\text{mag}} = 1.25(25) \chi_m H_0$. See also data for U^{15}N [70KV].

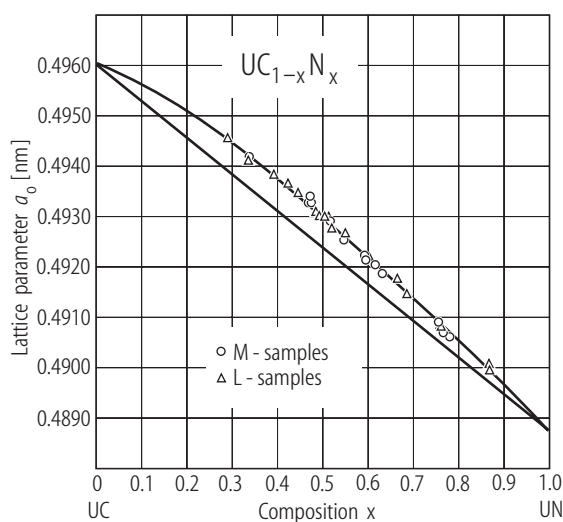


Fig. II.79. U(C,N) . The RT lattice parameter, a_0 , vs. nitrogen concentration, x , of the solid solutions $\text{UC}_{1-x}\text{N}_x$ for two sample series which were obtained by heating mixtures either of UN and UC (M-samples) or UN and graphite (L-samples) [75C]. Using for the lattice parameters of the end compounds UC and UN the values 0.49602 and 0.48880 nm, respectively, an equation describing the deviation from Vegard's relationship (solid curve through the experimental points) was proposed (see the text of original paper) and compared to another one presented earlier by [69LPSL]. See also [59WS].

For Fig. II.78 see next page

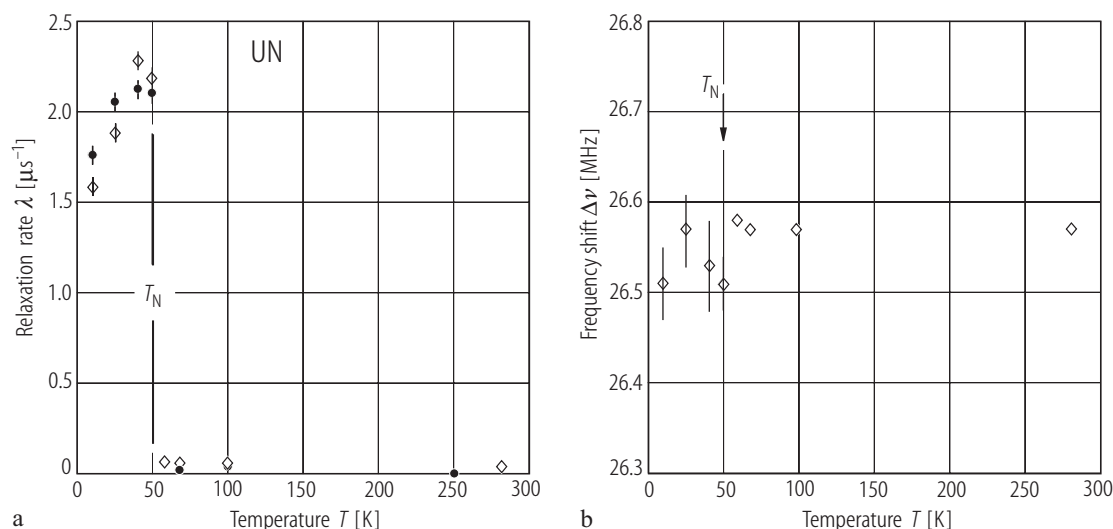


Fig. II.77. UN. (a) The muon spin relaxation (μSR) rate, λ , vs. T in transverse fields (TF) of 0.1 (closed circles) and 0.2 T (open diamonds) and (b) the frequency shift $\Delta\nu$ (in a TF of 0.2 T) vs. T [93MKKA]. Note that while a sudden drop in λ at T_N is well marked, no apparent change in $\Delta\nu$ occurs.

Also no trace of a magnetic precursor is seen from both these quantities. The static nature of minor spin depolarization (the half-width of the field distribution stays practically constant at $T < T_N$) confirms the AF $1-1\mathbf{k}$ magnetic structure of UN.

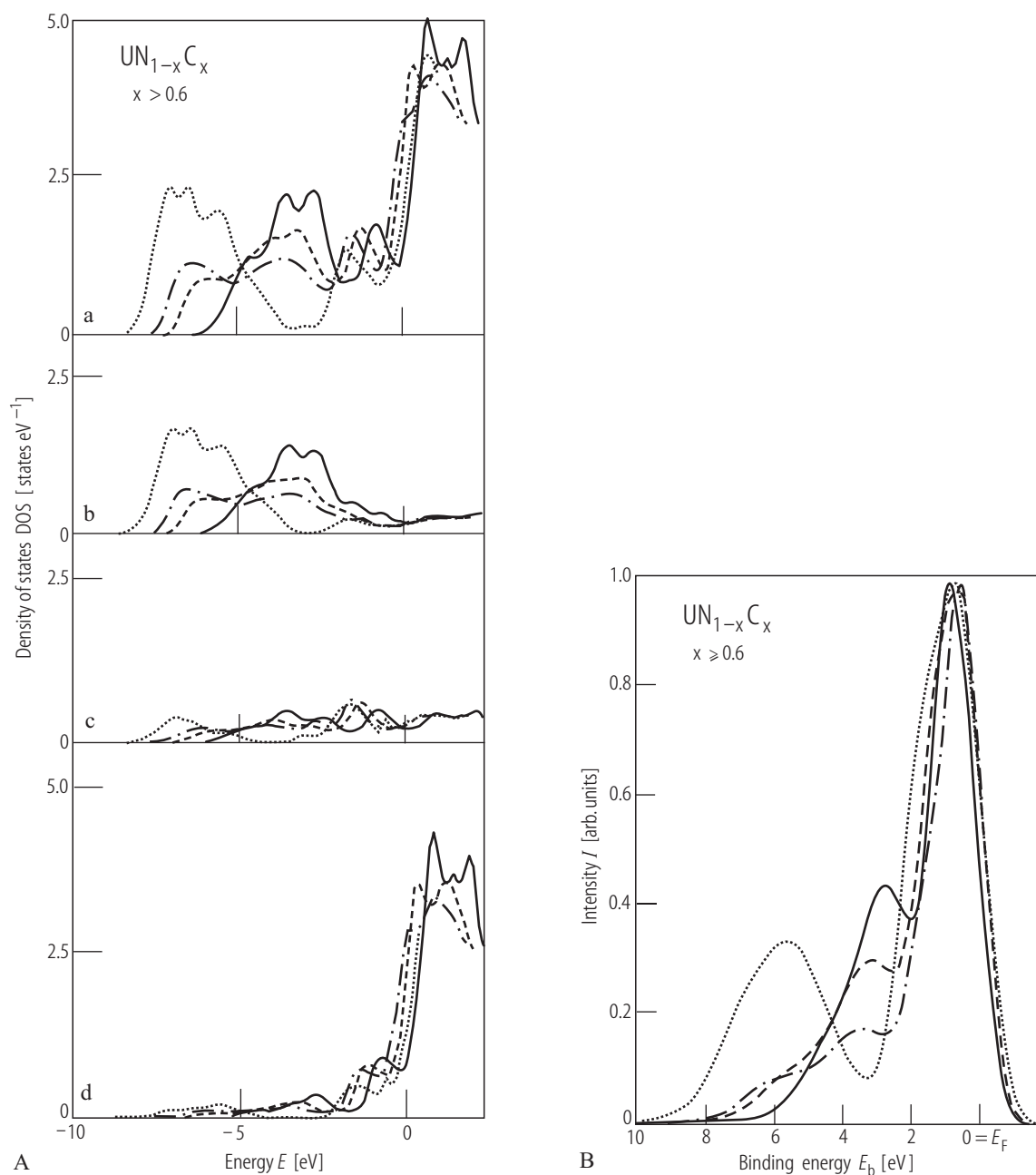


Fig. II.78. $\text{U}(\text{C}_x\text{N})$. **(A)** DOS of the solid solutions $\text{UN}_{1-x}\text{C}_x$ ($x > 0.6$) found in electronic structure calculations with RKKR – Gr method combined with CPA [91SM]: **(a)** Total DOS, **(b)** nonmetal site projected DOS, **(c)** U 6d partial DOS and **(d)** U 5f DOS for $\text{UN}_{1-x}\text{C}_x$, where $x = 1$ (solid line), $x = 0.8$ (dashed line), $x = 0.6$ (dot-dashed line) and $x = 0$ (dotted line). In accordance to [83BK], E_F lies close to a minimum of the DOS. $\gamma_b = 2.95 \text{ mJ/K}^2\text{mol}$ compared to a

measured $\gamma(0)$ value of about $20 \text{ mJ/K}^2\text{mol}$ [63DCM] and [64HMM]. **(B)** Calculated XPS spectra (meaning of curves as above) [91SM]. One sees from these curves a negligible dependence on composition. Both peaks at low and high binding energy (BE) for $x = 0$ (pure UN) originate mainly from hybridized U 5f - 6d states. Note that for UC ($x = 1$) the high BE band is shifted towards E_F by $\sim 2.5 \text{ eV}$.

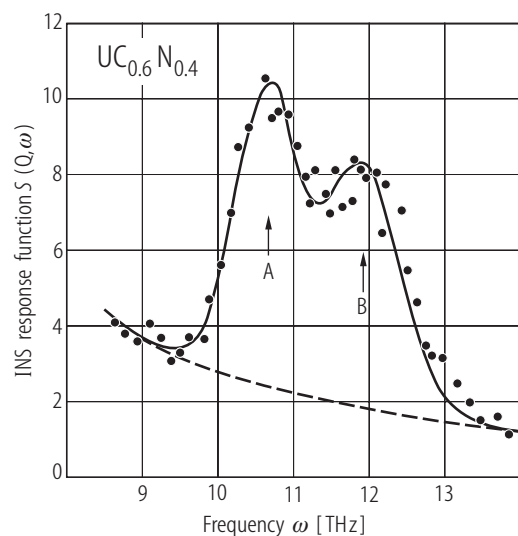


Fig. II.80. U(C,N). The scattering function, $S(Q, \omega)$, against frequency, ω , for the solid solution $\text{UC}_{0.6}\text{N}_{0.4}$ [78WDM]. Optic phonon modes are split into two peaks A and B corresponding respectively to local vibrations of carbon and nitrogen, which form the two-mode system. The solid line is a superposition of two Gaussians with centers at 10.70(5) THz, for C and 11.95(5) THz for N which can be compared to frequencies of pure UC (10.8(1) THz) and UN (11.8(1) THz) [74W].

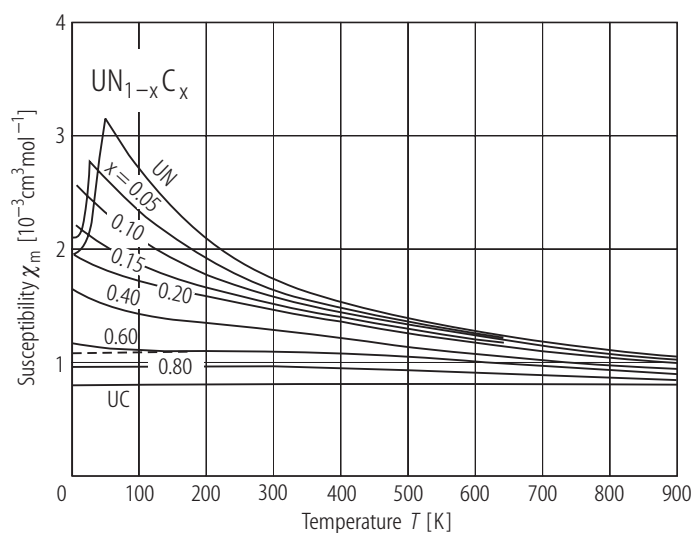


Fig. II.81. U(N,C). Molar magnetic susceptibility, χ_m , vs. T measured up to 900 K for the solid solutions $\text{UN}_{1-x}\text{C}_x$ where $0 \leq x \leq 1$ [72DC]. The samples with $x = 0.0$ ([70ON] and [70DC]), 0.04, 0.09 [72DC] are antiferromagnetic at $T_N = 52$ and 31 K, respectively. The data for UC, $\chi_m \approx 0.8 \cdot 10^{-3} \text{ cm}^3/\text{mol}$, were taken from [64BU].

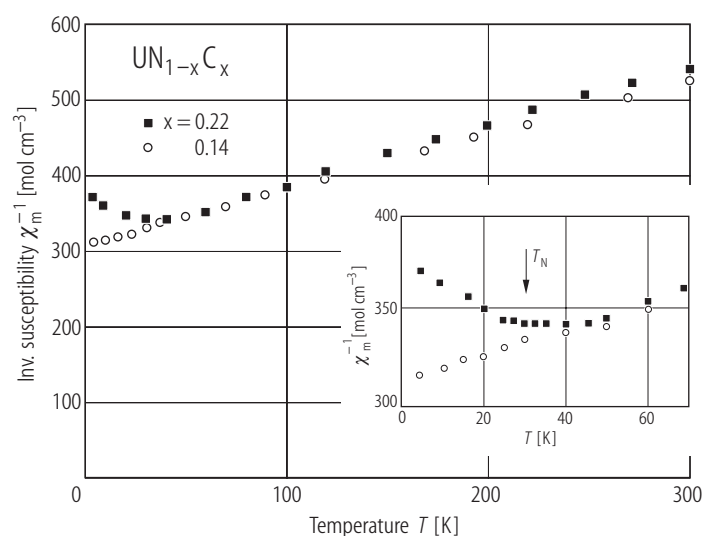


Fig. II.82. U(C,N). Inverse magnetic susceptibility, χ_m^{-1} , vs. T for two carbon concentrations $x = 0.22$ (closed squares) and 0.14 (open circles) of the solid solutions $\text{U}(\text{N}_{1-x}\text{C}_x)$ [74LLRM]. $\Theta_p = -420$ K and $p_{\text{eff}} = 3.2(1) \mu_B/\text{U atom}$ for both samples. The inset shows the low-temperature behaviour of χ_m^{-1} vs. T for the above two solid solutions.

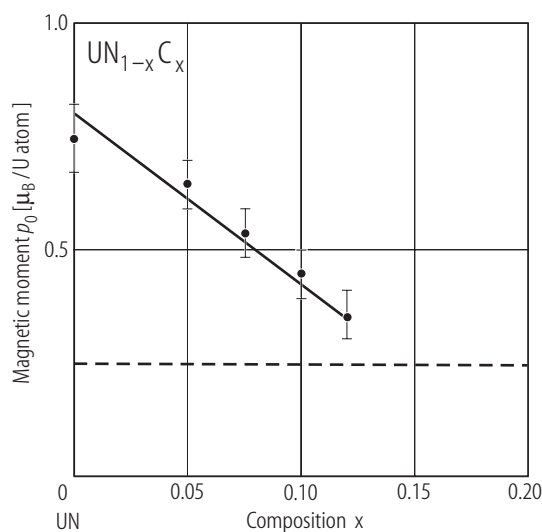


Fig. II.83. $U(N,C)$. The ordered magnetic moment, p_0 , vs. carbon concentration, x , for the solid solutions $UN_{1-x}C_x$ [74LLRM]. The dashed line shows a limit in the magnitude of magnetic moment determination by neutron diffraction.

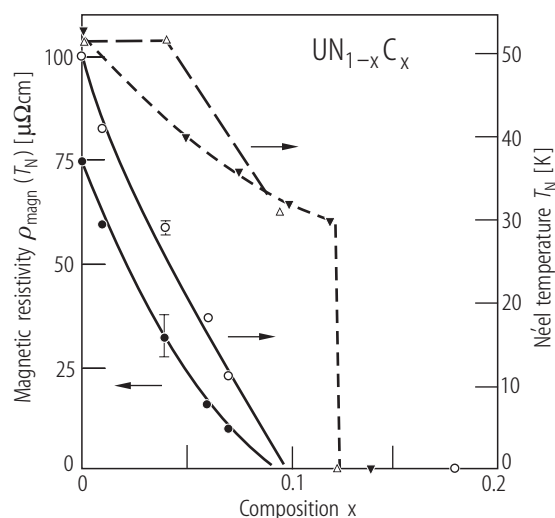
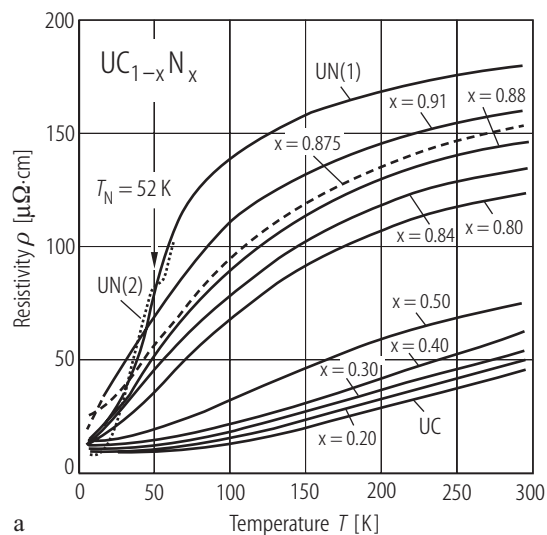
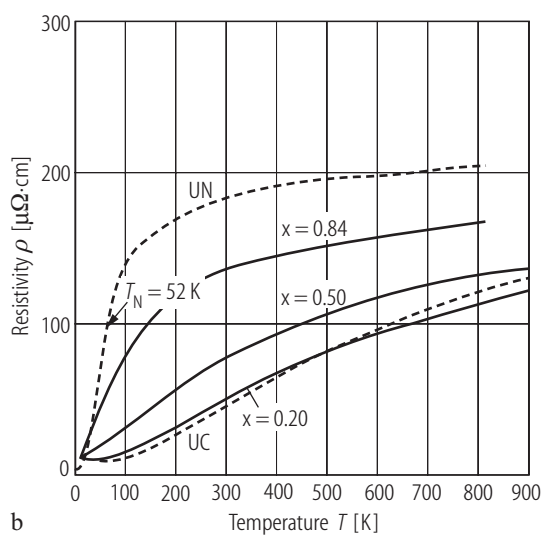


Fig. II.86. $U(N,C)$. Néel temperature, T_N , (open circles) and the magnetic resistivity at T_N , $\rho_{\text{mag}}(T_N)$, (closed circles) as a function of concentration, x , in the solid solutions $UN_{1-x}C_x$ [83TMMK]. For comparison there are also data of T_N vs. x of previous studies by [72DC] (open triangles) and by [74LLRM] (full triangles).



a



b

Fig. II.84. $U(N,C)$. Electrical resistivity, ρ , vs. concentration, x , for the solid solutions UN_xC_{1-x} at temperatures: (a) 4...300 K and (b) 4...900 K [72DC]. The data for UN(1), UN(2) and UC are from [64CLAR] and

[64CL], respectively. Compare the results in figure (b) with those given by [72OKN] for $0.3 \leq x \leq 1.0$ at temperatures 4...1100 K (not shown here) possessing about 85 % theoretical density.

For Fig. II.85 see next page

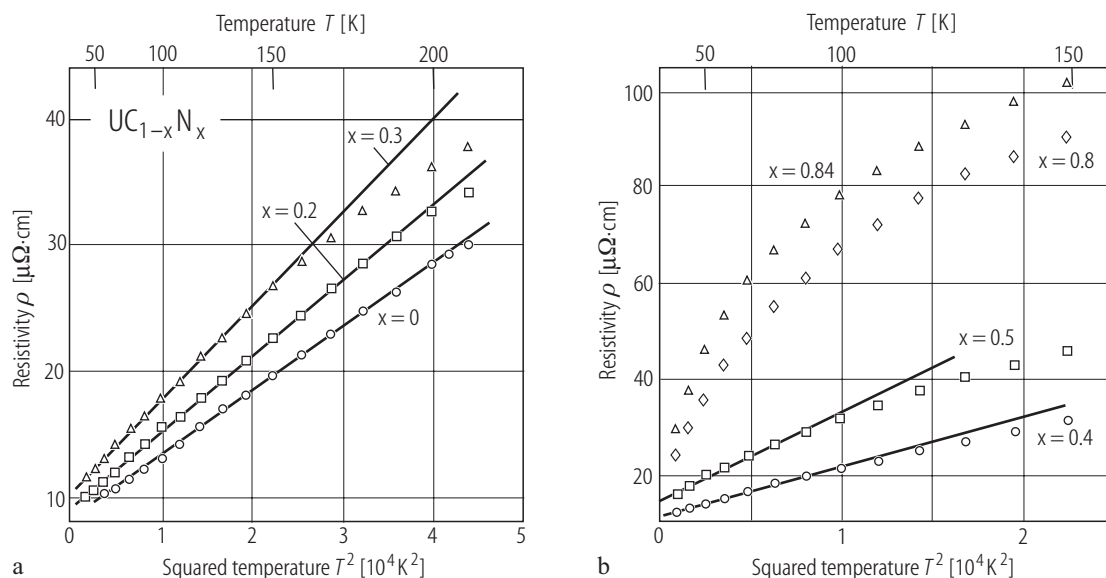


Fig. 11.85. $\text{U}(\text{N},\text{C})$. The electrical resistivity, ρ , vs. T^2 for the solid solutions $\text{UN}_x\text{C}_{1-x}$ with x indicated: (a) $x \leq 0.3$ and (b) $x \geq 0.4$ [78B]. The straight-line behaviour of this dependence points out the strong spin-fluctuation effect ($T_{\text{sf}} \sim 300 \text{ K}$) for the carbon-rich compositions.

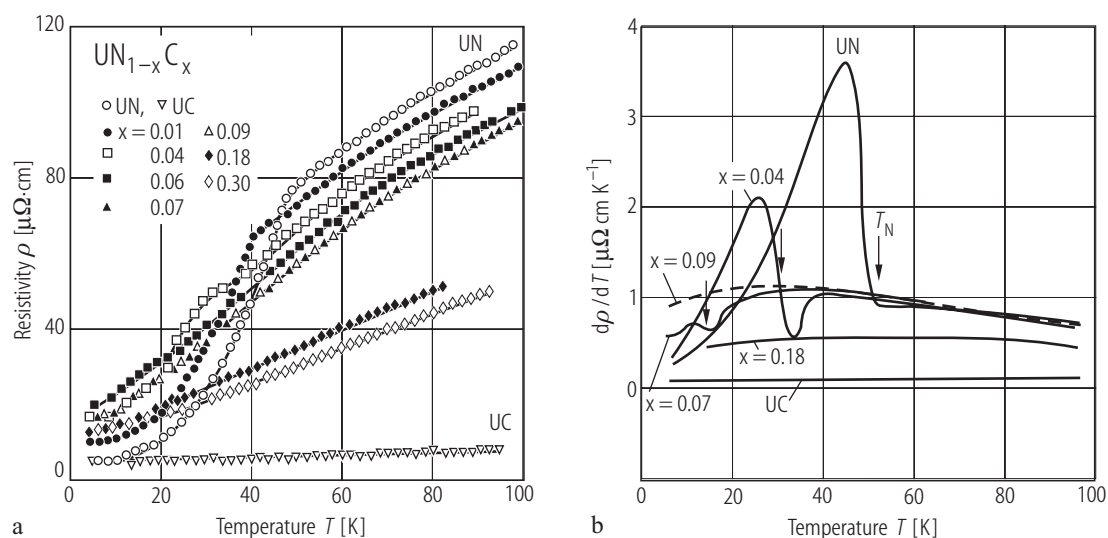


Fig. 11.87. $\text{U}(\text{N},\text{C})$. (a) Low-temperature electrical resistivities of UN and the solid solutions $\text{UN}_{1-x}\text{C}_x$ with: $x = 0.01, 0.04, 0.06, 0.07, 0.09, 0.18, 0.30$ and UC . (b) The temperature derivatives, $d\rho(T)/dT$, vs. T for $x = 0.0, 0.04, 0.07, 0.09, 0.18$ and 1.0 [83TMMK].

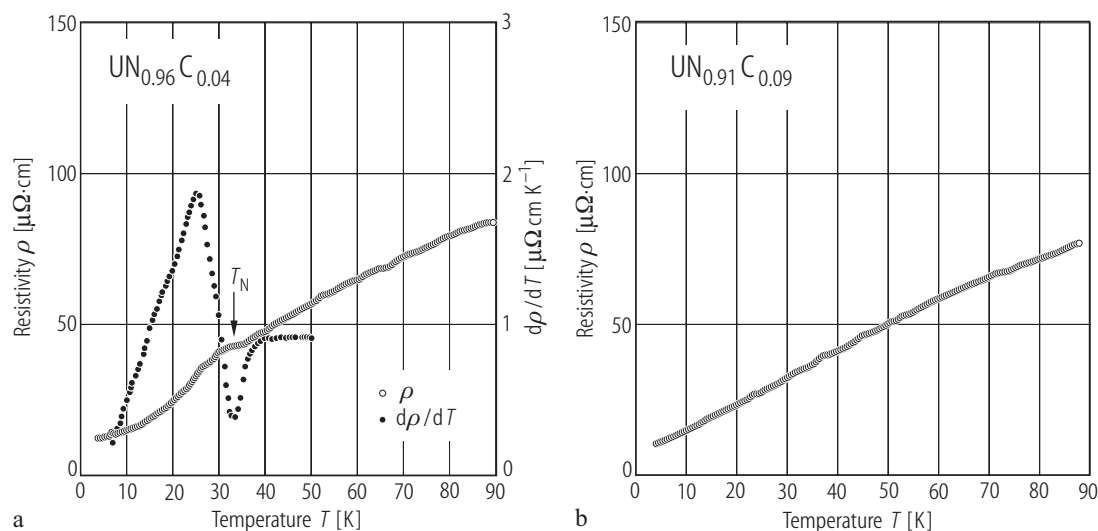


Fig. II.88. U(N,C). (a) Temperature dependences of the resistivity, ρ , and its derivative, $d\rho/dT$, for the solid solution $\text{UN}_{0.96}\text{C}_{0.04}$. $T_N \approx 31$ K [76NKMT]. (b) ρ vs. T for $\text{UN}_{0.91}\text{C}_{0.09}$. No “knee” is seen on this dependence indicating the lack of magnetic order [76NKMT]. Compare this behaviour with that presented in Fig. II.86 of [74LLRM].

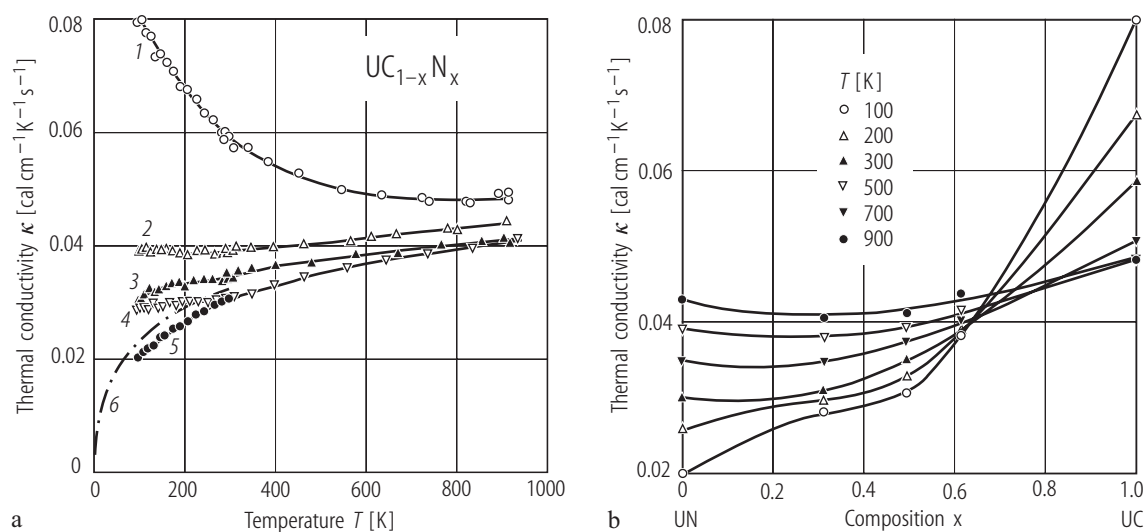


Fig. II.89. U(N,C). Thermal conductivity, κ , (a) of the solid solutions $\text{UN}_x\text{C}_{1-x}$, where x is 0 (curve 1), 0.39 (2), 0.51 (3), 0.69 (4) and 1.0 (5 and 6) as a function of temperature and (b) of the solid solutions $\text{UN}_{1-x}\text{C}_x$ vs. composition x at various temperatures from 100 to 900 K for the same compositions [74KTM2]. The data of (6) are from [69RW] and [70MFM].

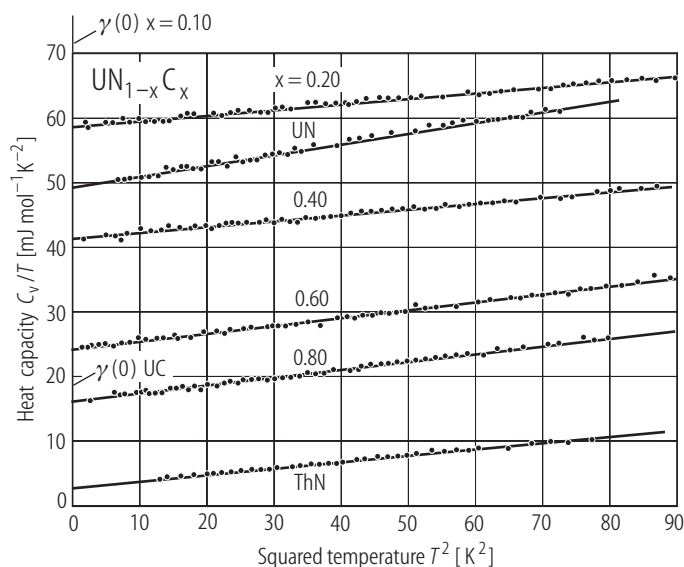


Fig. II.90. $U(N,C)$, (ThN). The C_v/T vs. T^2 plot for ThN and the solid solutions $UN_{1-x}C_x$ based on the data obtained between 1.3 and 10 K [70DC],[72DC]. Given also for ThN $\gamma(0) = 3.12$ mJ/mol K^2 and $\Theta_D = 284$ K. For UN these values are: 49.6 mJ/mol K^2 and 234 K, respectively. A marked $\gamma(0)$ value for UC ($\gamma(0) = 18.6$ mJ/mol K^2) is from [64HMM]. For $\gamma(0)$ vs. x dependence see Fig. II.91.

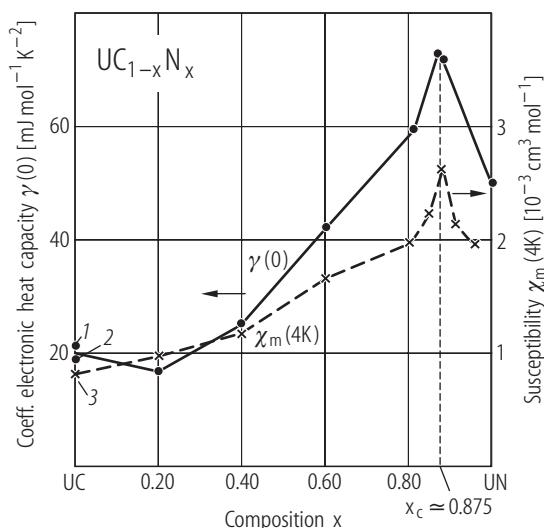


Fig. II.91. $U(C,N)$. The composition dependences of $\gamma(0)$ and $\chi_m(4.2$ K) for the solid solutions $UC_{1-x}N_x$ [72DC]. In both cases the maximum values for both these quantities are obtained at the critical concentration $x_{cr} = 0.875$ where the magnetic order vanishes. Numbers 1 and 2 mark the data of $\gamma(0)$ given by [64HMM] and [63DCM], while 3 is for $\chi_m(4.2)$ given by [64BU].

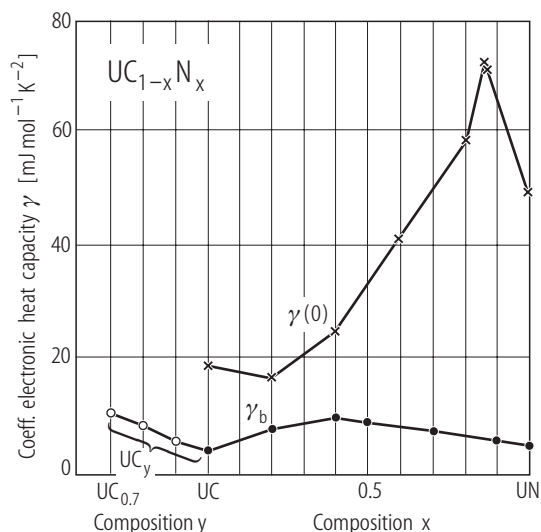


Fig. II.92. $U(C,N)$. Experimental linear specific heat coefficient, $\gamma(0)$, [72DC] and theoretical, γ_b , as a function of the composition, x , in solid solutions $UC_{1-x}N_x$ and for the UC_y ($y > 0.7$) [91SM]. Band calculations by RKKR (Gr) method.

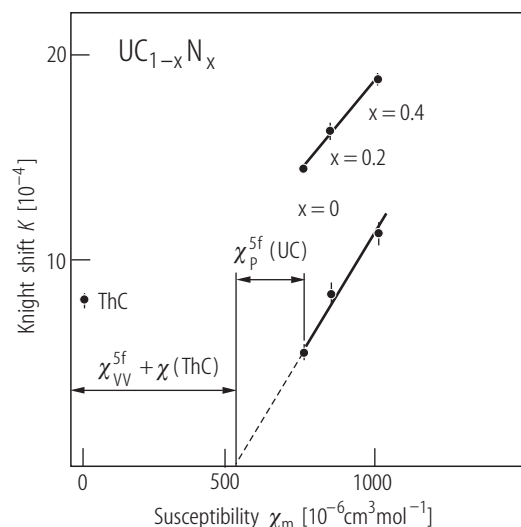


Fig. II.93. U(C,N). (ThC). Knight shift, K , of ^{13}C in the solid solutions $\text{UC}_{1-x}\text{N}_x$ ($x = 0, 0.2, 0.4$) as a function of the susceptibility, χ_m , (upper line) and the separated contact term K_C (5f) vs. χ^{5f} (lower line) [76BD]. On a 5f band model χ^{5f} is the difference ($\chi - \chi_{\text{orb}}$) where $\chi_{\text{orb}} = 500 \cdot 10^{-6} \text{ cm}^3/\text{mol}$. In this model χ_{orb} is also described as the Van Vleck contribution χ_{vv} independent of the temperature. Note a positive value of K for Th^{13}C ($8.0(3) \cdot 10^{-4}$) compared to a negative value of $(-2.2 \cdot 10^{-4})$ reported by [68LRKW], which were obtained on the ^{13}C enriched and non enriched in samples, respectively.

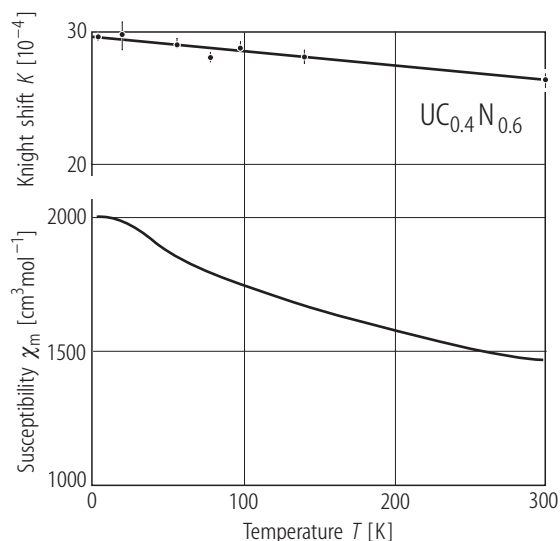


Fig. II.94. U(C,N). The Knight shift, K , of ^{13}C in $\text{UC}_{0.4}\text{N}_{0.6}$ (upper curve) and the molar susceptibility, χ_m , (lower curve) as a function of temperature [76BD]. The temperature change for these quantities between 4.2 and 300 K is only 10 and 25 %, respectively. The much slower temperature dependence of $K(T)$ compared to $\chi(T)$ originates from the fact that the RKKY contribution to the ^{13}C Knight shift is only a small part of the total value.

For Fig. II.95 see next page

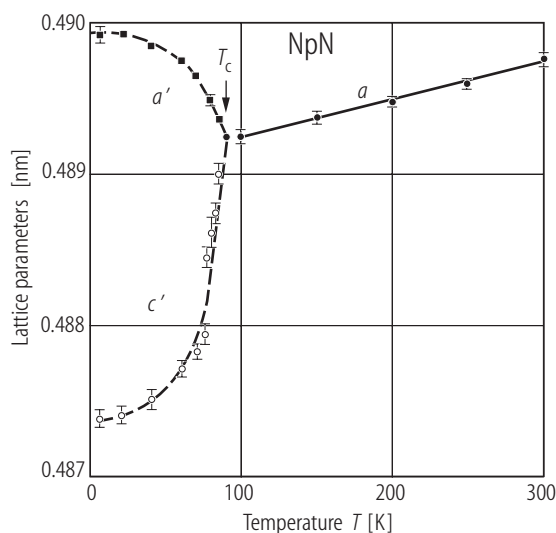


Fig. II.96. NpN. Lattice parameters as a function of temperature [74MLKR]. The parameters a' and c' correspond to the trigonal phase stable below T_C ($= 87 \text{ K}$). At 5 K the value of $(c' - a')/a' = -52 \cdot 10^{-4}$ (for definition see Table 9).

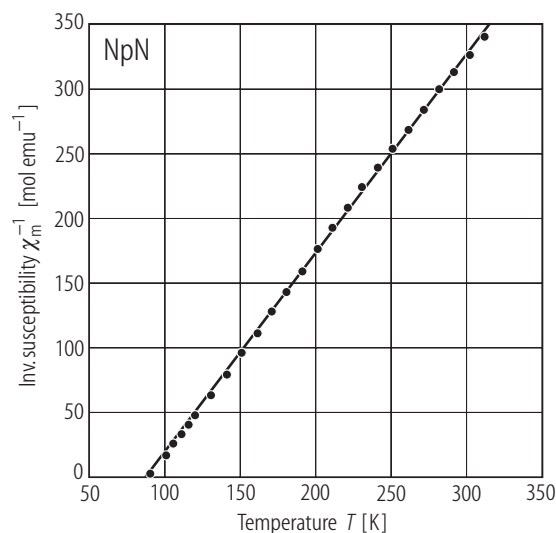


Fig. II.97. NpN. Inverse molar magnetic susceptibility, χ_m^{-1} , vs. temperature, T , [74ADHL]. $\Theta_p = 100(10) \text{ K}$, $p_{\text{eff}} = 2.4 \mu_B/\text{Np at.}$ (shown in LB III/12c, p.434, Fig.60).

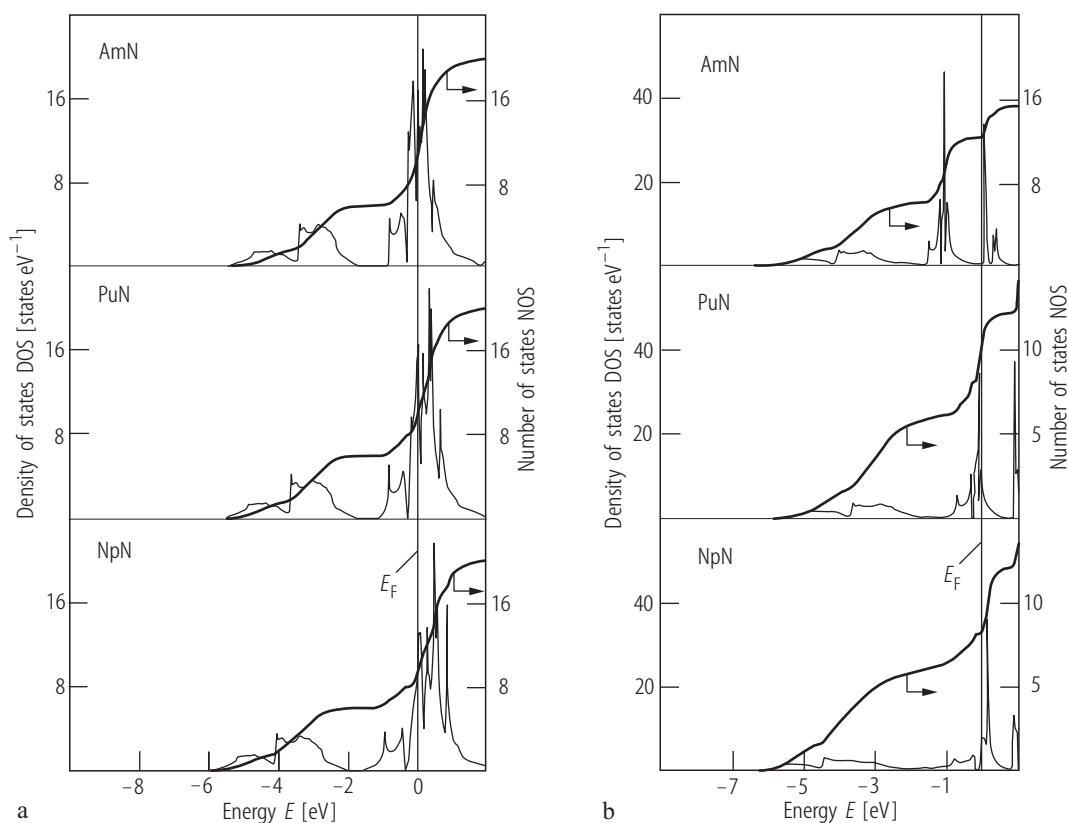


Fig. II.95. AnN (An = Np, Pu, Am). Total density of states, DOS (lhs) and number of states, NOS, (rhs), from **(a)** LMTO- (modified Pauli equation) and **(b)** RLMTO- calculations (Dirac equation) [84B3] and [86BJES]. The Fermi level is at the zero of energy. For the total density of states

at the Fermi level for both kinds of calculations see the Table under Fig. II.3. The spin-orbit coupling is responsible for the remarkable changes in electronic structure between LMTO and RLMTO methods.

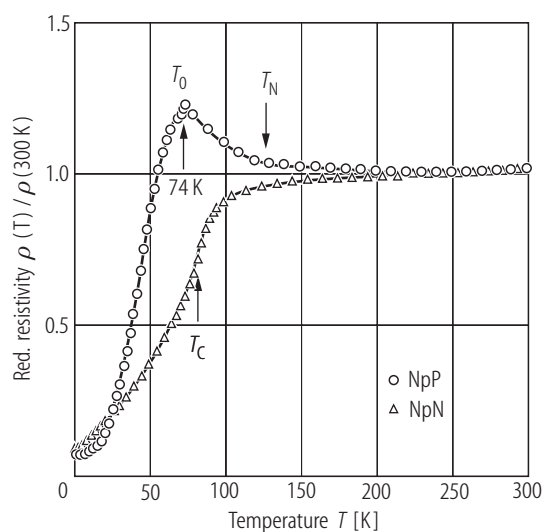


Fig. II.98. NpN, NpP. Reduced electrical resistivity, $\rho(T)/\rho(300 \text{ K})$, vs. temperature, T , [74ADHL]. The corresponding transition temperatures, T_C ($= 87(3) \text{ K}$) and T_0 ($= 74 \text{ K}$) preceding T_N ($= 130(3) \text{ K}$) for NpN and NpP, respectively, are marked by arrows. (LB III/12c, p.484, Fig. 61). $\rho(300) = 3100 \mu\Omega\text{cm}$.

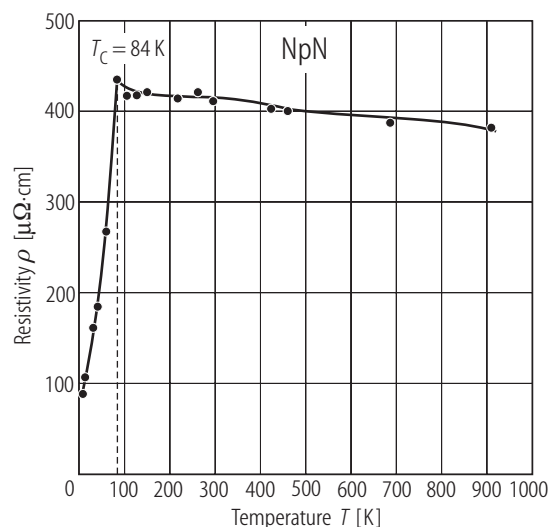


Fig. II.99. NpN. Electrical resistivity, ρ , vs. T up to 900 K [68DL]. $T_C = 84$ K. Due to the large porosity of the sample, for which the density was estimated to be only 74 % compared to the theoretical one, the data seem to be unreliable. Hence, the real resistivity should show considerably lower values.

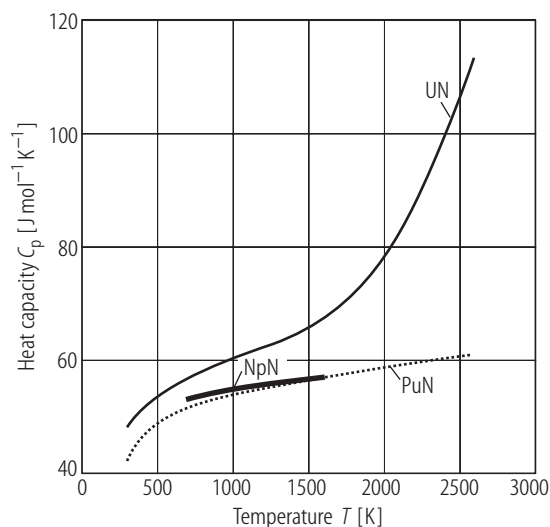


Fig. II.100. AnN. Heat capacity, C_p , vs. T of the actinide mononitrides: UN, NpN, PuN measured in the temperature range 300...2600 K by different authors (see [98SA]). For C_p of NpN between 740...1600 K see ref. [94AOS] and between 350...1000 K ref. [02NA]. For UN, see also Fig.II.73.

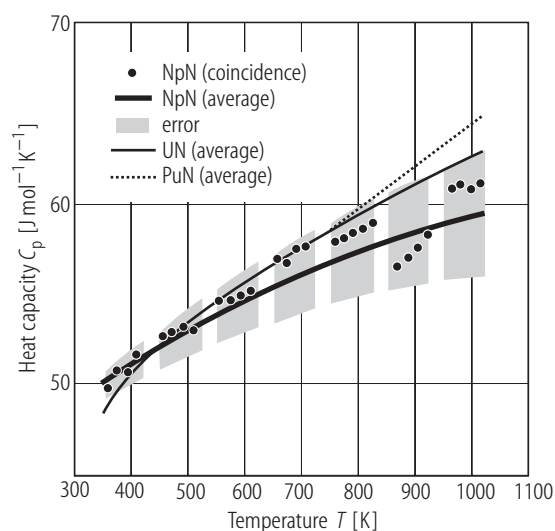


Fig. II.101. NpN. Heat capacity, C_p , vs. temperature, T , measured from 350 to 1000 K for NpN [02NA] and compared to UN and PuN taken from [72OL] and [78O], respectively.

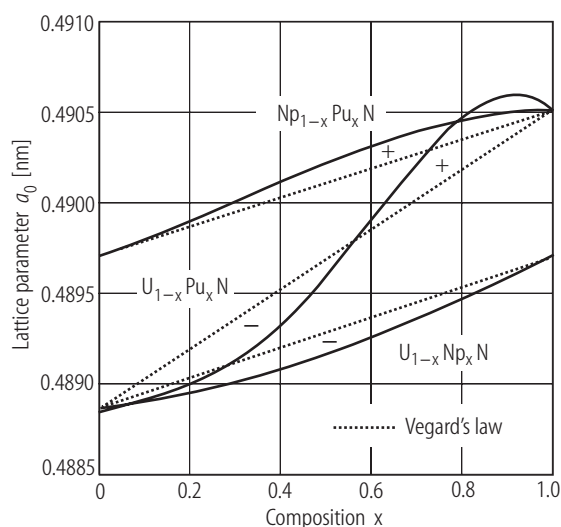


Fig. II.102. (An,An')N. Lattice parameters, a_0 , at RT against concentration, x , for the solid solutions: $U_{1-x}Np_xN$, $U_{1-x}Pu_xN$ and $Np_{1-x}Pu_xN$ [98SA]. Note the deviation from Vegard's law, negative in UN–NpN and UN-rich compositions with PuN and positive in NpN–PuN and PuN-rich compositions with UN.

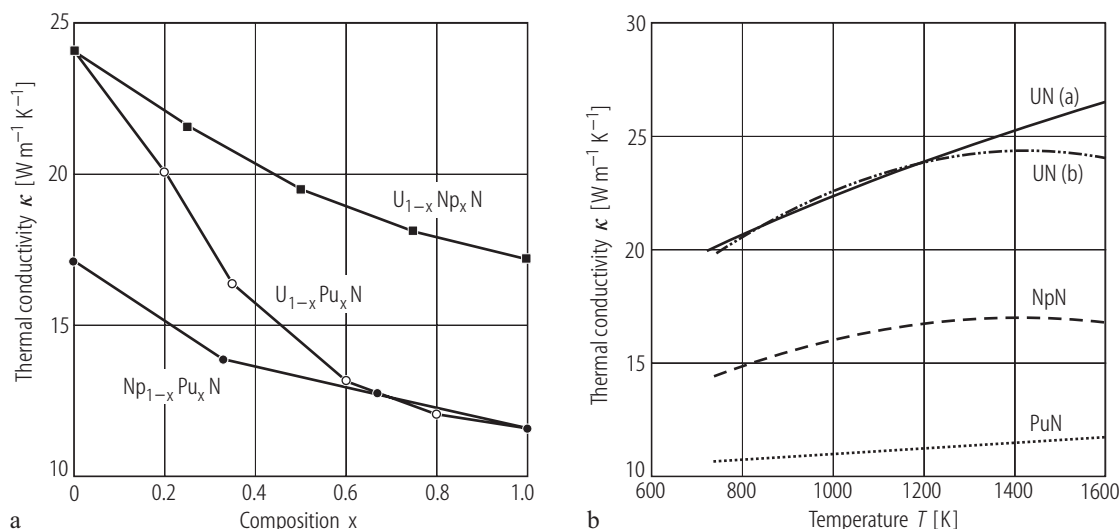


Fig. II.103. (An, An')N, AnN; An = U, Np, Pu. **(a)** Thermal conductivity, κ , as a function of concentration, x , for the indicated solid solutions $(\text{An}_{1-x}\text{An}'_x)\text{N}$ at 1273 K [98SA]. **(b)** Thermal conductivity, κ , vs. T for 1. UN **(a)** [90HTP3] and UN **(b)** [92ASIO], NpN [94AOS] and PuN [92ASIO] at temperatures between 700...1600 K compiled by [98SA].

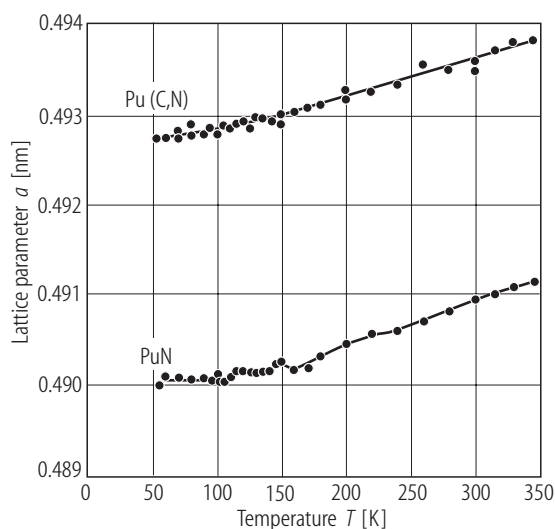


Fig. II.104. PuN, Pu(C,N). Lattice parameter, a , vs. temperature, T , measured between 50 and 345 K [78BDS]. Chemical analysis gave $\text{PuN}_{0.89}$ and $\text{PuC}_{0.28}\text{N}_{0.56}$ with some oxygen contamination. In contrast to the earlier works reporting particular features in the curves of length change, expansion coefficient, magnetic susceptibility, electrical resistivity and specific heat versus temperature (for references see [78BDS]) for these materials no phase transformations were observed in the temperature dependence of the lattice parameter.

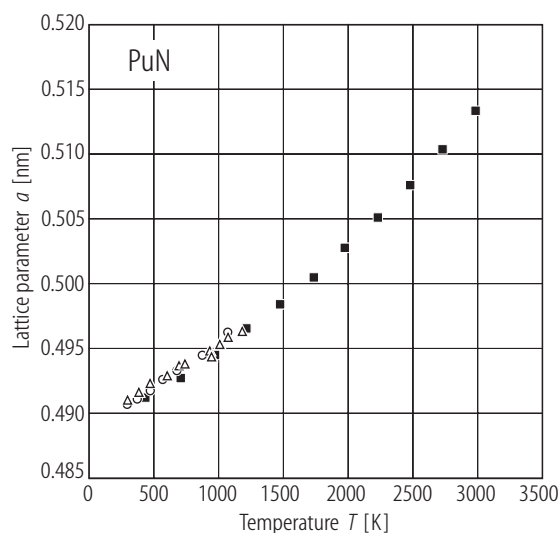


Fig. II.105. PuN. Lattice parameter, a , vs. T determined at temperatures between 300 and 3000 K by MD calculations (closed squares) [00KYYU2] together with experimental data (open circles) [63C] and open triangles [62RS] measured between 300 and 1200 K.

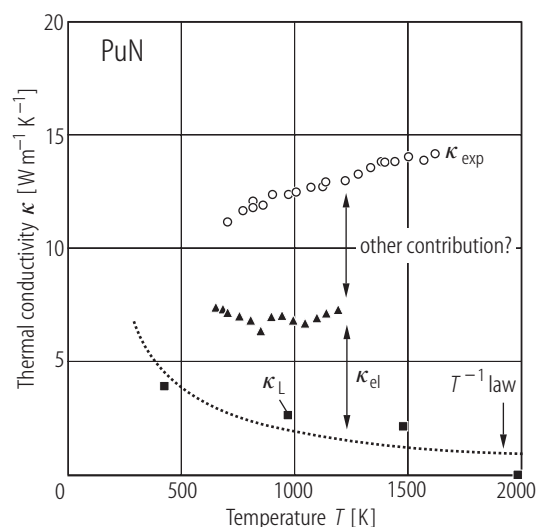


Fig. II.106. PuN. Thermal conductivity, κ , vs. T (open circles) measured between 700 and 1700 K [92ASIO], compared to the lattice thermal conductivity κ_L evaluated by MD calculations between 300 and 2000 K [00KYYU2]. The electronic contribution κ_{el} evaluated by the Wiedemann-Franz law, was added to κ_L , yielding the data marked as closed triangles. The difference between κ_{exp} and the sum $\kappa_L + \kappa_{el}$ indicates the possible other contribution to the total thermal conductivity not yet specified [00KYYU2].

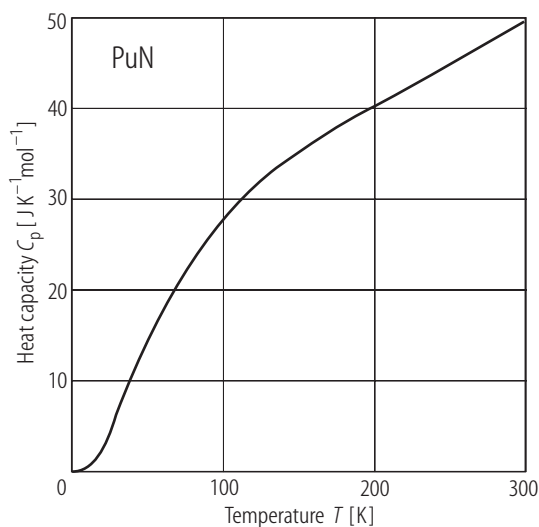
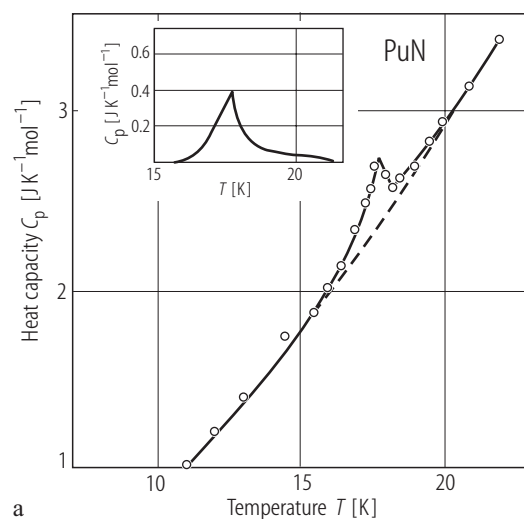
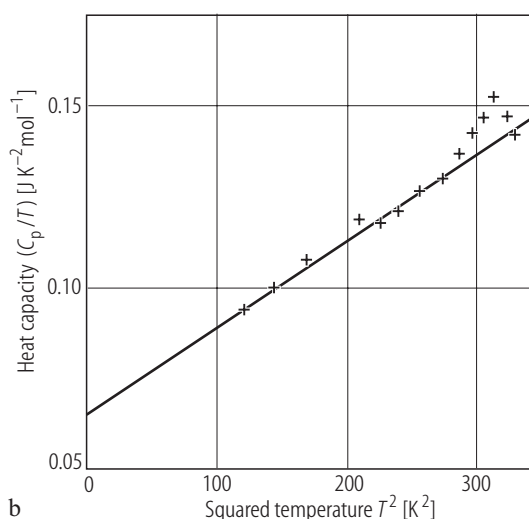


Fig. II.108. PuN. Heat capacity, C_p , vs. temperature, T , between 10 and 300 K, taken four years later after the C_p measurements of PuN shown in Fig. II.107a [78HLMM]. Note that the anomaly at 18 K had been eliminated due to the radiation damage, so that the thermodynamic quantities given in this paper are applicable only to a self-damaged PuN.



a



b

Fig. II.107. PuN. **(a)** Heat capacity, C_p , vs. temperature, T , between 11 and 22 K [78HLMM]. $a_0 = 0.49046(4)$ nm. See the anomaly at 17.8(2) K, higher than that at 13(1) K found from the susceptibility measurements (given by [69RD]).

The inset shows the difference between measured C_p and smooth interpolation in the region of anomaly. **(b)** The C_p/T vs. T^2 plot over the temperature range 10 to 16.5 K [78HLMM]. $\Theta_D = 255(5)$ K, $\gamma(0) = 66(4)$ mJ/K²mol.

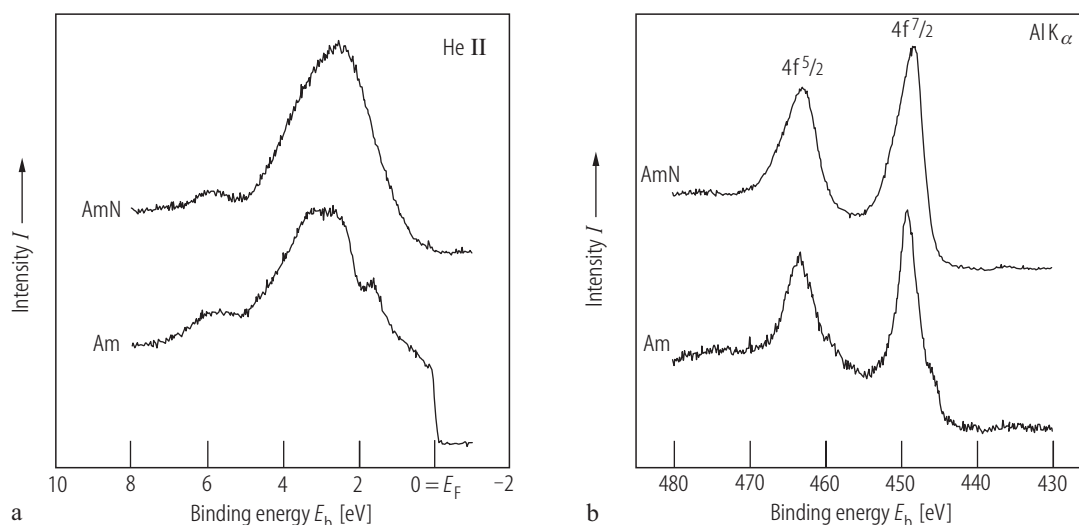


Fig. II.109. AmN, Am (thin films). **(a)** The HeII photoelectron spectrum measured on films of Am metal and AmN [05GOHW]. Am has a clear valence band contribution at 0 eV, which is not observed for AmN. Therefore AmN is either an insulator or has a pseudo-gap at the Fermi energy. **(b)** The 4f core XPS spectra of AmN film compared to Am film measured with Al K α radiation

[05GOHW]. Am metal shows a weak so-called well-screened shoulder at lower binding energies, which in turn completely disappears for AmN, indicating that there are no delocalised valence electrons present in AmN at the Fermi energy to provide screening. For energy-band structure of AmN computed with the LDA and LDA+ U approach at the experimental lattice parameters see [05GDOB].

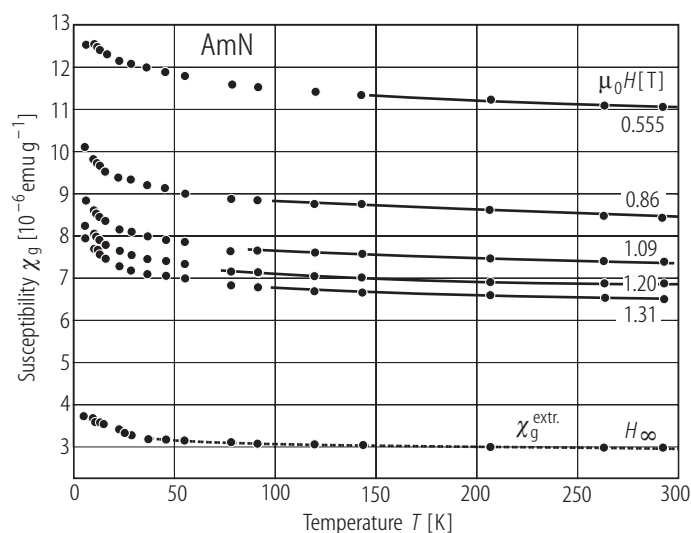


Fig. II.110. AmN. Specific magnetic susceptibility, χ_g , vs. temperature, T , measured in various magnetic fields as indicated [76KMM]. Extrapolation of $\chi_g(H)$ to infinite field strength gives $\chi_g = 3.05 \cdot 10^{-6}$ emu/g which corresponds to $\chi_m = 777(3) \cdot 10^{-6}$ emu/mol.

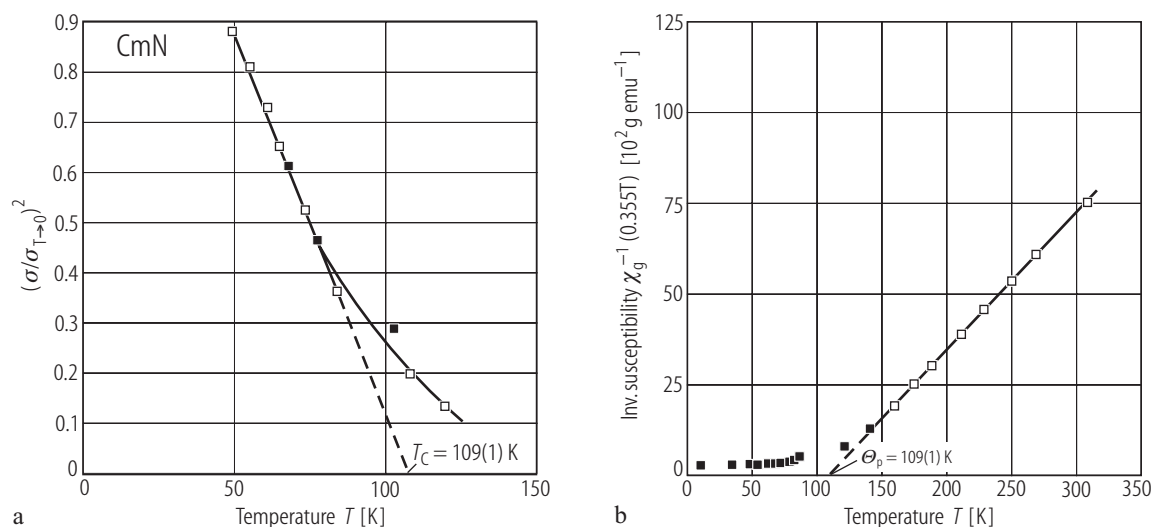


Fig. II.111. CmN. **(a)** The ratio of squared magnetizations, $(\sigma(T)/\sigma_{T \rightarrow 0})^2$, vs. temperature, T , [76KCMM]. Extrapolation of this ratio to zero (dashed line) defines the Curie temperature $T_C = 109(1)$ K. **(b)** Inverse specific susceptibility, χ_g^{-1} , vs. temperature, T , [76KCMM]. $p_{\text{eff}} = 7.02 \mu_B$, $T_C \equiv \Theta_p = 109(1)$ K. See also Table 2.

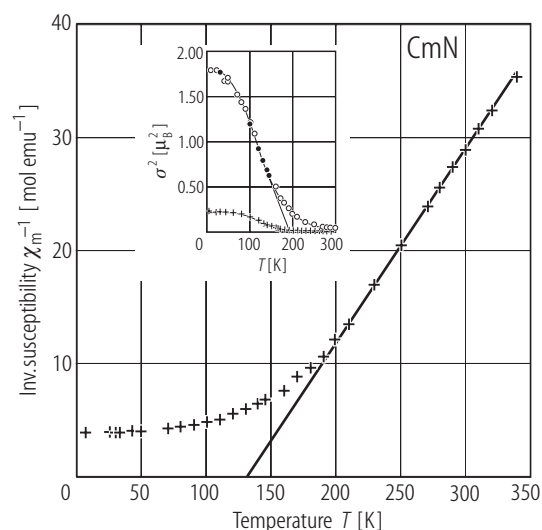


Fig. II.112. CmN. Inverse molar susceptibility, χ_m^{-1} , vs. temperature, T , measured at 3 T [87HN]. The Curie-Weiss fit marked by the solid line yields $p_{\text{eff}} = 6.8 \mu_B$ and $\Theta_p = 129$ K. The effective moment is smaller than the free Cm^{3+} ion one of $7.55 \mu_B$. The inset shows squared magnetization, σ^2 , vs. T measured at two magnetic fields of 0.5 T (crosses) and 3 T (open circles). The saturation moment, p_s , is about $1.7 \mu_B$ at 5 T. Compare these data with those given in [76KCMM]. See also Table 2.

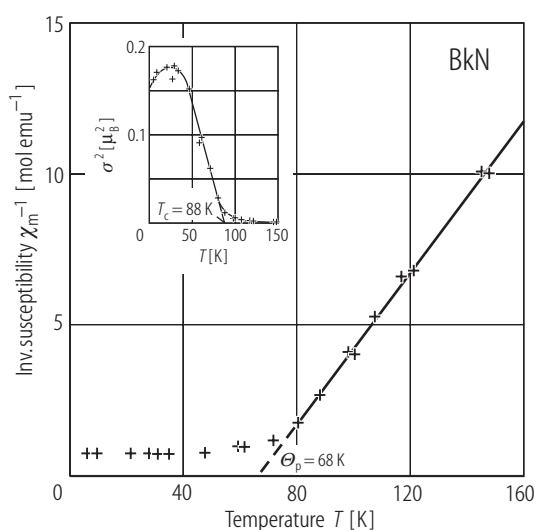


Fig. II.113. BkN. Inverse molar susceptibility, χ_m^{-1} , vs. temperature, T , measured at 1.6 T up to 150 K [87HN]. The solid line is the Curie-Weiss fit at limited temperature range of 80...150 K, which gives $p_{\text{eff}} = 7.9 \mu_B$ and $\Theta_p = 68$ K. The p_{eff} value is between the values of the f^7 ($7.55 \mu_B$) and f^8 ($\sim 9.3 \mu_B$) configurations. The inset gives the square of the magnetization, σ^2 , as a function of temperature taken at 0.16 T. An extrapolation of σ^2 to 0 (solid line) determines T_C ($= 88$ K). See also Table 2.

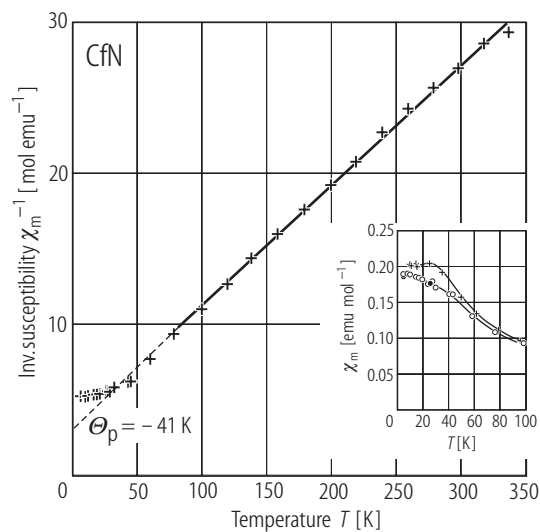


Fig. II.114. CfN. Inverse molar magnetic susceptibility, χ_m^{-1} , vs. temperature, T , up to 330 K [86NMHP]. The solid line is the Curie-Weiss fit with the values $p_{\text{eff}} = 10.3 \mu_B$ and $\Theta_p = -41 \text{ K}$. See also Table 2. The inset gives the χ_m vs. T dependence taken at two applied magnetic fields: 0.5 T (crosses) and 3 T (open circles) [87HN].